Assessment of Convectively Generated Tropical Cirrus in Global Storm-Resolving Models

Jacqueline Nugent

A thesis
submitted in partial fulfillment of the
requirements for the degree of

Master of Science

University of Washington

2021

Committee:

Christopher Bretherton, Chair

Thomas Ackerman

Alex Anderson-Frey

Peter Blossey

Program Authorized to Offer Degree:
Atmospheric Sciences

University of Washington

Abstract

Assessment of Convectively Generated Tropical Cirrus
in Global Storm-Resolving Models

Jacqueline Nugent

Chair of the Supervisory Committee:
Professor Christopher Bretherton
Department of Atmospheric Sciences

Pervasive cirrus clouds in the upper troposphere and tropical tropopause layer (TTL) influence the climate by altering the top-of-atmosphere radiation balance and stratospheric water vapor budget. These cirrus are often associated with deep convection, which global climate models must parameterize and struggle to accurately simulate. By comparing high-resolution global models from the DYAMOND intercomparison that explicitly simulate deep convection to satellite observations, we assess how well these models simulate deep convection, convectively generated cirrus, and deep convective injection of water into the TTL over representative tropical land and ocean regions. The DYAMOND models simulate deep convective precipitation, organization, and cloud structure fairly well over land and ocean regions, but with clear inter-model differences. All models produce frequent overshooting convection whose strongest updrafts humidify the TTL and are its main source of frozen water. Inter-model differences in cloud properties and convective injection exceed differences between land and ocean regions in each model. We argue that global storm-resolving models can better represent tropical cirrus and deep convection in present and future climates than coarser-resolution climate models. To realize this potential, they must use available observations to perfect their ice microphysics and dynamical flow solvers.

TABLE OF CONTENTS

LIST OF FIGURES

LIST OF TABLES

ACKNOWLEDGMENTS

I would like to thank my advisor, Chris Bretherton, for his invaluable advice and guidance throughout my graduate studies so far. I wish to thank Tom Ackerman and Peter Blossey for their extensive discussions and direction for this research and Sami Turbeville for her collaboration. I also want to thank Alex Anderson-Frey for her feedback on this work. Additionally, I would like to thank Adam Sokol and Blaž Gasparini for their insights and help with obtaining and analyzing the DARDAR and CCCM data.

Funding for this work was provided by the National Science Foundation through the Partnerships in International Research and Education program under grant number OISE-1743753. The broader PIRE Cirrus research team has been a source of knowledge and support for the past three years of my studies and I want to express my gratitude to the other members. DYAMOND data management was provided by the German Climate Computing Center (DKRZ) and supported through the projects ESiWACE and ESiWACE2, which have received funding from the European Union's Horizon 2020 research and innovation program under grant agreements No. 675191 and 823988. I want to thank the DKRZ team members for their help with accessing and managing the DYAMOND output.

Finally, I would like to thank my family, my cohort, and my friends in and outside of Seattle for all of their support and encouragement.

Chapter 1

INTRODUCTION

Upper-tropospheric cirrus influence the climate through local radiative heating. These cirrus extend throughout the tropics and can be advected up to 1000 km during their long lifetimes (Luo & Rossow, 2004). Jensen et al. (1996a) found that very thin cirrus can warm the surrounding atmosphere by a few Kelvins per day. Due to the prevalence of the cirrus, this heating alters the top-of-atmosphere radiation balance (Lee et al., 2009; Haladay & Stephens, 2009).

Tropical cirrus in the upper troposphere are strongly related to deep convection. Areas with a high occurrence of cirrus clouds are often collocated with frequent convection (e.g., Lee et al., 2009; Sassen et al., 2009; Schoeberl et al., 2018). Near the tropopause, cirrus can form through convective anvil detrainment as well as in situ ice nucleation (Jensen et al., 1996b). Some of the cirrus formed in situ may also be related to convection if the ice nucleation results from cooling caused by gravity wave perturbations (Dessler et al., 2006; Jensen et al., 2016). Pervasive, mostly optically thin cirrus characterize the transition region between the upper troposphere and lower stratosphere, known as the tropical tropopause layer (TTL; see review article by Fueglistaler et al., 2009). Several definitions for the TTL boundaries have been proposed in the literature; here, we take the TTL to be the 14–18 km layer in the tropics. The formation and maintenance of TTL cirrus are of particular interest to us. Like other upper-tropospheric cirrus, TTL cirrus are associated with deep convection. Overshooting convection that reaches into the TTL is especially important for TTL cirrus as it injects water vapor and ice crystals into the layer to support cirrus formation (e.g., Massie et al., 2002; Luo & Rossow, 2004; Mace et al., 2006; Krämer et al., 2016) and can ultimately alter the TTL composition (Fierli et al., 2011; Virts & Houze, 2015). Additionally, Jensen

et al. (1996a) determined that cirrus near the tropopause formed outside of convection act to dehydrate the stratosphere. Both TTL cirrus and changes in stratospheric water vapor concentrations radiatively impact large-scale upper-atmospheric circulations and the global climate (Solomon et al., 2010).

Overshooting convection drives water transport into the upper troposphere and is a major issue for global climate models (GCMs) in simulating tropical cirrus clouds (Fueglistaler et al., 2009). Deep convection is not resolved by the typical GCM horizontal grid spacings of 25–200 km and must be parameterized, which is notoriously challenging due to the complex small-scale structure of deep convection. The parameterizations inevitably lead to substantial biases and inter-model differences in simulated deep convection and related clouds. For instance, most GCMs simulate the diurnal cycle of convection over land poorly, with a maximum in precipitation often occurring too early in the day (Yang & Slingo, 2001; Khairoutdinov et al., 2005; Chao, 2013). An accurate diurnal cycle is needed to simulate tropical cirrus because the timing of anvil detrainment may affect the cirrus characteristics and thus their radiative effects (Sokol & Hartmann, 2020). Land convection is particularly important for TTL cirrus because it penetrates the TTL more often (Liu & Zipser, 2005) and is more intense than ocean convection (Yang & Slingo, 2001; Zipser et al., 2006). However, different convective parameterizations in GCMs disagree on the representation of convective fluxes and often struggle to reproduce convection that overshoots the cold point (Arteta et al., 2009).

Cloud-resolving models (CRMs) have sufficiently fine horizontal grid spacings to explicitly resolve deep convection without parameterization. An early CRM study by Bechtold et al. (2004) found that the precipitation maximum over tropical land realistically shifted to later in the day with nonparameterized deep convection. This improvement in the simulated diurnal cycle has been reproduced by numerous studies (e.g., Duda & Gallus, 2013; Berthou et al., 2019).

Increased computing power has since allowed for the development of global storm-resolving models (GSRMs), global CRMs of 1-5 km horizontal grid resolution, that can resolve indi-

vidual convective storms. Recently, several GSRMs were brought together as part of the Dynamics of the Atmospheric general circulation Modeled On Nonhydrostatic Domains (DYAMOND) project (Stevens et al., 2019). The DYAMOND project provides a novel opportunity for the intercomparison of TTL cirrus and convection modeled at such high resolutions. Because of the expected improvements from explicitly simulating deep convection, the DYAMOND models have the potential to more accurately model tropical cirrus in the upper troposphere and TTL in a changing climate. But is this potential realized, even in the present climate that we can observe? Other parameterizations still needed in GSRMs, especially ice microphysics, could still be major sources of model error. GSRM fidelity in accurately simulating strong grid-scale convective updrafts and downdrafts also needs to be assessed.

The goal of this work is to use a variety of observations, mainly from satellites, over representative land and ocean regions to assess how well tropical deep convection and convectively generated cirrus are simulated in the DYAMOND GSRMs. The remainder of this thesis is organized as follows: Chapter 2 provides an overview of the methods, including descriptions of the models, datasets, and study regions. We assess the fidelity of the DYAMOND models in simulating both land and ocean convection in Chapter 3. We examine the differences in the model output of microphysical variables related to cirrus in Chapter 4. In Chapter 5, we relate deep convection to the simulated cirrus by analyzing the convective injection of water vapor and ice into the TTL. Chapter 6 concludes the thesis with a discussion of the results, their implications for our understanding of modeling tropical cirrus, and directions for future work.

Chapter 2

METHODS AND DATA

2.1 DYAMOND Models

The DYAMOND initiative brought together nine different GSRMs with 5 km or finer horizontal grid spacing and explicit, nonparameterized deep convection (Stevens et al., 2019). These GSRMs each have their own specific design described in detail in Stevens et al. (2019), but all models were initialized from the same meteorological analysis and run freely for a total of 40 days from 1 August to 10 September 2016. In addition to the high spatial resolution, the DYAMOND GSRMs also have high temporal resolution, with output saved every 15 minutes for 2D fields and every 3 hours for 3D fields.

Our analysis focuses primarily on the four models: NICAM, FV3, ICON, and SAM (starred models in Table 2.1). Hereafter we refer to these models collectively as NFIS. This limited subset of models allows for a detailed, in-depth evaluation of such high resolution simulations while maintaining a manageable output volume. To place the NFIS models into context with the rest of the intercomparison, we also evaluate the output of certain 2D fields for the other DYAMOND models: IFS, ARPNH, MPAS, and UM (Table 2.1). We have omitted the ninth model, the Goddard Earth Observing System (GEOS), because the saved DYAMOND run included a poor implementation of its microphysics scheme that distorted the model results (Putman, 2020).

We have analyzed the NFIS models at their native grid scales where possible; however, some interpolation was necessary for ICON and FV3. ICON output is saved on an icosahedral grid, so for spatial plots all variables were first interpolated via nearest neighbors onto the finest latitude-longitude grid permitted by the number of cells. For FV3, the 3D hydrometeor profiles, 2D integrated water paths, and pressure were regridded through first-

Table 2.1: Name and horizontal grid spacing for the eight DYAMOND models used in this study. We focus on the first four (starred) but use the other four for comparisons of certain 2D variables.

Model Name	Abbreviation	Horiz. Grid Spacing (km)
Non-hydrostatic Icosahedral Atmospheric Model	NICAM*	3.5
Finite-Volume Cubed-Sphere Dynamical Core	FV3*	3.25
Icosahedral Non-hydrostatic Model	ICON*	2.5
Global System for Atmospheric Modeling	SAM*	4
Integrated Forecast System	IFS	5
ARPEGE-NH	ARPNH	2.5
Model for Predicting Across Scales	MPAS	3.8
United Model	UM	7.8

order conservative remapping onto a regular latitude-longitude grid while all other variables were saved on the native cubed sphere grid. These regridded variables had a larger number of cells in the study regions than the native variables, so for any analysis involving both types, all variables were first aligned onto a new latitude-longitude grid through nearest neighbors interpolation. In addition, FV3 uses a hybrid pressure-sigma vertical coordinate and the altitude was only saved on a limited number of pressure levels. We calculated a regional-mean altitude of all model levels from horizontal regional averages of pressure, temperature, and specific humidity by integrating the hypsometric equation up from the known horizontal-mean surface elevation and pressure.

Most DYAMOND models have one-moment microphysics schemes, which partition the frozen water into cloud ice, snow, and graupel. Unlike the models, satellite measurements generally cannot distinguish between the types of frozen hydrometeors. The observed "ice" is most accurately compared to the total sum of what each model defines as cloud ice, snow, and graupel, which we refer to here as the total frozen water. In addition to the 3D profiles of cloud ice, all models except ARPNH and UM saved output for the 2D column-integrated

ice water path (IWP), snow water path (SWP), and graupel water path (GWP), whose sum we call the frozen water path (FWP). However, NICAM is the only model that also saved the 3D output of snow and graupel, so we can only directly compare 3D profiles of the observed frozen water content (FWC) to NICAM output. Chapter 4 further discusses the implications of this limitation.

Finally, we have omitted the first 48 hours of each model from any averaging or sampling to avoid contamination from the spin-up period, which includes an initial shock in precipitation in NICAM. Therefore, "time-mean" refers to the average of days 3–40 in each DYAMOND model run (i.e., 3 August to 10 September).

2.2 Datasets

Since the DYAMOND models were run freely, they will not reproduce specific, observed weather systems after the first few days. Therefore, we assess model fidelity by comparing time means and distributions of their output to a set of observational and reanalysis data from the same time of year.

We take FWC measurements from DARDAR-CLOUD v2.1.1, which combines radar and lidar retrievals from CloudSat and CALIPSO (Delanoë & Hogan, 2008, 2010). These satellites, part of NASA's A-Train constellation, cross the equator at approximately 01:30 and 13:30 local time for nighttime and daytime measurements, respectively (Stephens et al., 2002). The combination of radar and lidar data in DARDAR (raDAR-liDAR) capitalizes on the detection strengths of both instruments to enable retrievals in areas of deep convection as well as thin cirrus. The DARDAR data have a horizontal grid spacing of approximately 1.1 km and 60 m vertical grid spacing (e.g., Sokol & Hartmann, 2020). We use FWC retrievals from July-August-September (JAS) 2009 to correspond to the DYAMOND season, which were then vertically integrated to calculate the observed frozen water path (FWP). Although solar noise increases the uncertainty in lidar measurements during the day, we include both daytime and nighttime retrievals to avoid diurnal bias.

For precipitation, we build an 11-year climatology during the DYAMOND period by

merging estimates from 1 August to 10 September 2006–2016. We use the Tropical Rainfall Measurement Mission (TRMM) Multi-satellite Precipitation Analysis (TMPA) 3B42 version 7 product, which contains 3 hourly data at a spatial resolution of 0.25° (Huffman et al., 2007, 2010). This product combines microwave and infrared rainfall estimates with precipitation gauge measurements using the algorithm described by Huffman et al. (2007) with modifications for the current version detailed in Huffman and Bolvin (2018).

We obtain retrievals of outgoing longwave radiation (OLR) from the sun-synchronous Clouds and the Earth's Radiant Energy System (CERES) satellite for JAS 2007–2010. The CERES data are contained in the CALIPSO, CloudSat, CERES, and MODIS merged data product (CCCM) described by Kato et al. (2010, 2011). CERES has a ∼20 km footprint and also belongs to the A-Train constellation.

For temperature and humidity, we use the high-resolution European Center for Medium Range Weather Forecasts (ECMWF) Reanalysis v5 (ERA5) from 1 August to 10 September 2016. The ERA5 dataset contains global hourly output on 37 pressure levels at a resolution of 31 km regridded to 0.25° (Hersbach et al., 2020). We calculate the altitude of each pressure level from the ERA5 geopotential variable.

2.3 Study Regions

This study examines two representative $10^\circ \times 10^\circ$ latitude-longitude regions in the tropics as shown in Figure 2.1: a continental area over the Sahel (SHL) in western Africa and an oceanic area over the Tropical Western Pacific (TWP).

The Sahel region was chosen to represent tropical land for several reasons. This area experiences frequent deep convection during the DYAMOND period when the West African Monsoon is active. Furthermore, a large proportion of overshooting convection that extends above 14 km in the tropics occurs over Africa (Liu & Zipser, 2005). The Sahel region encompasses several different climate regions, from the moist and convectively active savanna to the Sahara desert, where detrained anvils are the main cloud type during the monsoon season (Futyan et al., 2004). Finally, this region is approximately centered over the African

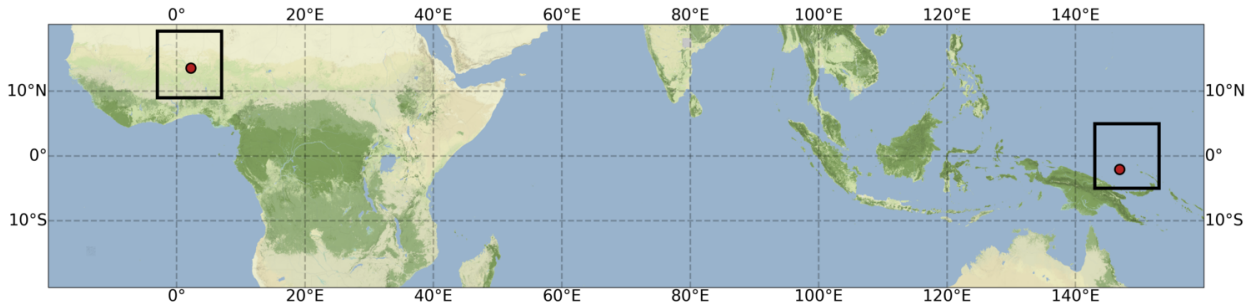

Figure 2.1: Locations of the analysis regions in (left) the Sahel, 3°W–7°E, 9°N–19°N; and (right) the Tropical Western Pacific, 143°E–153°E, 5°S–5°N. Red dots indicate locations of the (left) AMMA and (right) ARM sites.

Monsoon Multidisciplinary Analysis (AMMA) measurement site in Niamey, Niger, where the RADAGAST field campaign took place in 2006 (Slingo et al., 2008). RADAGAST generated a rich suite of measurements of the overlying atmospheric column that may in the future be climatologically compared with the DYAMOND output.

The TWP region contains frequent ocean convection, a valuable complement to the Sahel region. The TWP box is approximately centered over the Atmospheric Radiation Measurement (ARM) site in Manus, Papua New Guinea (Long et al., 2016).

2.4 Mass Flux Calculation

One goal of this study is to analyze how the DYAMOND models bring the ice and moisture into the TTL necessary to support cirrus cloud formation and maintenance. To this end, we examine the vertical advective mass fluxes of frozen water and water vapor at 14 km, a representative height of the TTL base. The mass fluxes (F, kg m^{-2} s^{-1}) of water vapor, frozen water, cloud ice, snow, and graupel are calculated in equation (2.1):

$$F = w\rho q^* \tag{2.1}$$

Here, w is the vertical velocity (m s^{-1}), ρ is the air density (kg m^{-3}), and q^* (kg kg^{-1}) is either the specific humidity for the water vapor flux or the specific water content (frozen,

cloud ice, snow, or graupel) for the other fluxes. The w used in equation (2.1) does not include any ice fall velocity, which was not an output archived by the models. We calculate the water vapor and cloud ice mass fluxes for all NFIS models. Since FV3, ICON, and SAM do not save the 3D model outputs of snow and graupel that are needed to determine the total FWC, we can only calculate the frozen water, snow, and graupel mass fluxes for NICAM.

2.5 Frozen Water Path Categorization

We will use the FWP to divide ice-containing air columns into three categories with distinct physical characteristics, following Sokol and Hartmann (2020):

Category 1: FWP ≥ 1000 g m^{-2} (deep convection)

Category 2: $10 \leq$ FWP < 1000 g m^{-2} (thick "anvil" cirrus)

Category 3: $0.1 \leq$ FWP < 10 g m^{-2} (thin cirrus).

The models can simulate cirrus layers so thin that lidar cannot distinguish them from clear sky. The lower threshold of Category 3 is chosen to exclude most such cirrus layers from our model-observation comparisons. It corresponds to a 200 m thick cirrus layer (narrower than the 400–600 m vertical grid spacing of the NFIS models within the TTL) with an average FWC of 5×10^{-4} g m^{-3}, which Deng et al. (2013) found to be the smallest value measurable by satellite-based lidar. Columns with FWP < 0.1 g m^{-2} are considered to be cirrus-free.

The SAM 2D water paths require additional processing. These files were saved with 2-byte compression that quantizes values into integer multiples of 1/64,000th of the field maximum. While IWP and LWP can be computed by integrating profiles of cloud ice and liquid in the 3D outputs, we statistically correct the errors due to quantization in the snow, graupel, and rain water paths by adding random perturbations to any values below 1 g m^{-2}.

Chapter 3

CONVECTION

In this chapter, we evaluate the performance of the DYAMOND models in simulating both land and ocean convection.

3.1 Thermodynamic Background

Since the DYAMOND models are not nudged towards observations, they each settle into their own climates over the course of the model run. We compare the model output for temperature and relative humidity to ERA5 reanalysis data in order to understand the mean thermodynamic state of each model. The relative humidity with respect to ice in the DYAMOND models was calculated using the equation for ice-saturation vapor pressure from Murphy and Koop (2005).

Despite their microphysical diversity, the models all simulate mean relative humidity profiles that scatter within ∼15% of ERA5 below the cold point and fall well within one standard deviation of the ERA5 daily mean (Figure 3.1c, d), which is not true of the temperature profiles. This disagreement in temperature but not relative humidity suggests that convection has a lasting influence on the TTL in the NFIS models. The mean temperature profiles alone do not explain the relative humidity profiles, so the infrequent periods of deep convection are likely acting to humidify the upper troposphere to around 70–90%, consistent with Ueyama et al. (2018).

3.2 Accumulated Precipitation

The DYAMOND models scatter around the observed accumulated precipitation in both regions, with generally higher precipitation over the TWP (Figure 3.2b) than the Sahel (Figure

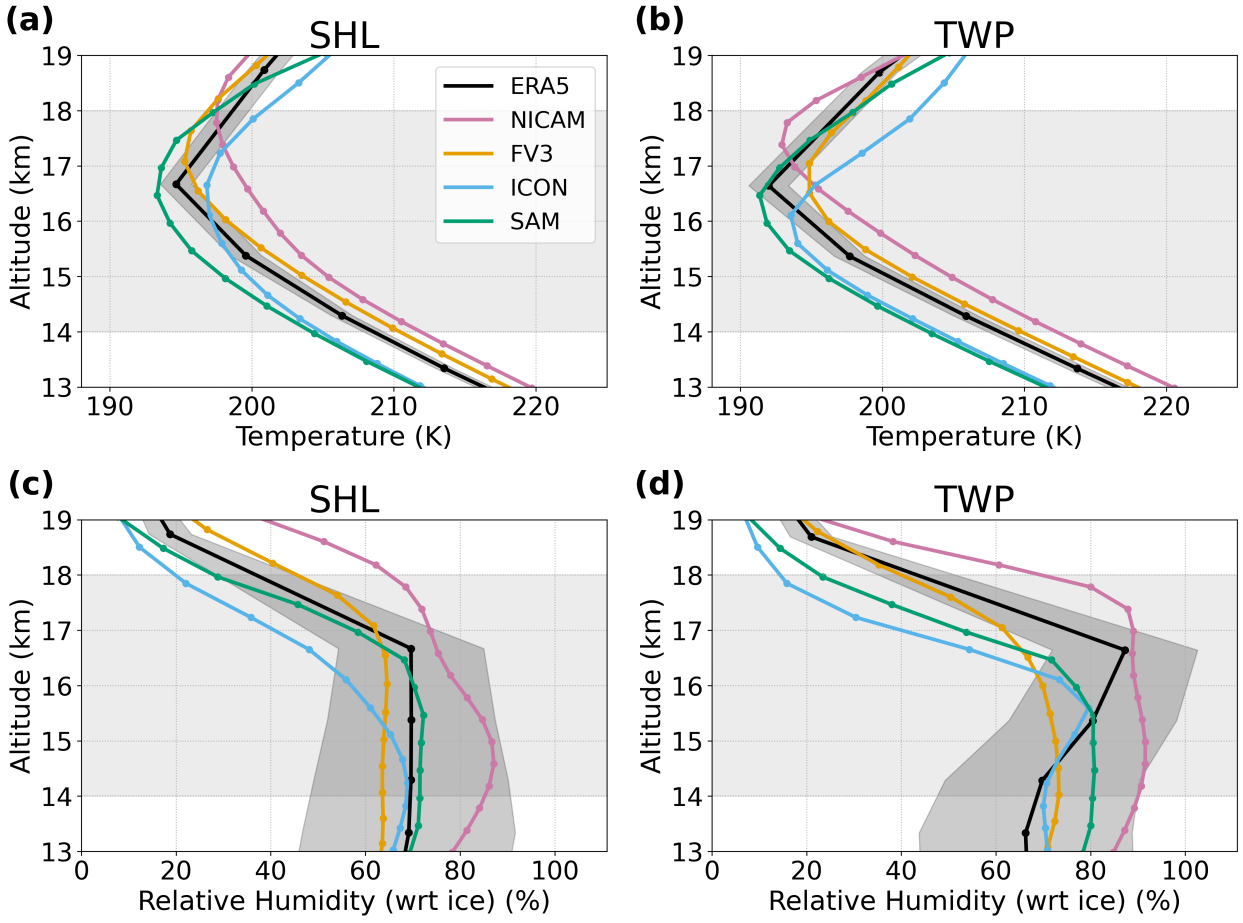

Figure 3.1: Time- and regional-mean vertical profiles of (top) temperature and (bottom) relative humidity with respect to ice for the (left) Sahel and (right) TWP for the NFIS models and ERA5 reanalysis data. The standard deviation of the daily mean ERA5 data is shaded in dark grey. The TTL is shaded in light grey.

3.2a). The ratio of TWP to Sahel 40-day accumulated precipitation ranges considerably from 1.0 (ARPNH, IFS) to 3.6 (UM), compared to an 11-year TRMM climatological estimate of 1.6 for the DYAMOND period in 2006–2016. Since the models are free-running and a 40-day average is short, this ratio may not be fully representative of each model's climatological behavior, but Figure 3.2 suggests some models systematically precipitate more than others in each region.

The DYAMOND models as a whole reasonably simulate the total precipitation in both

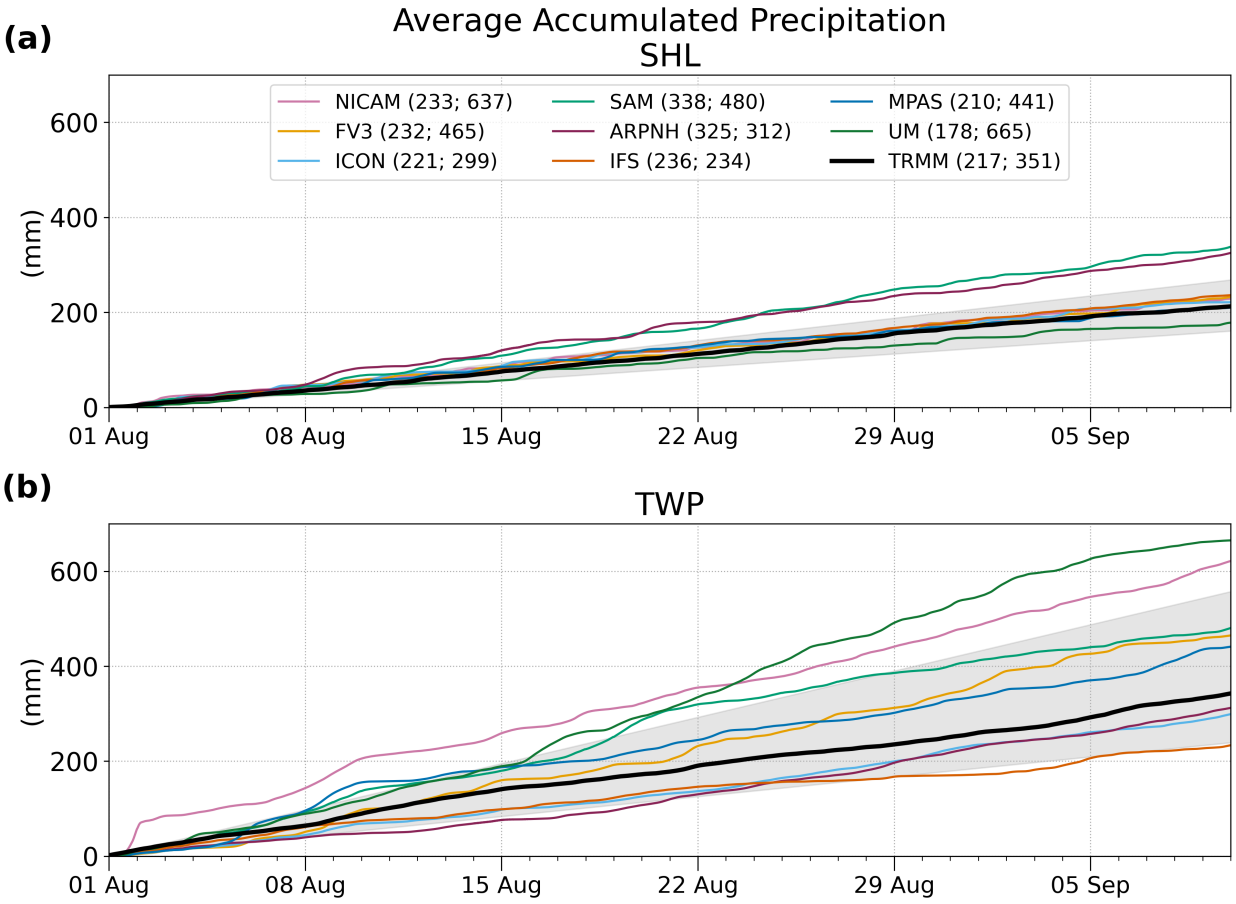

Figure 3.2: Regional-mean accumulated precipitation at each time step for the (a) Sahel and (b) TWP. The black line represents the 2006–2016 TRMM climatological average accumulation during the DYAMOND time period. The grey shading shows the range in accumulation observed by TRMM over this 11-year period. The numbers in the legend are the 40-day accumulations in (left) the Sahel and (right) the TWP in mm.

regions with most model accumulation falling within the 11-year TRMM climatological range. Among the NFIS models, none simulate precipitation notably better than the others. SAM consistently accumulates about 50% more precipitation than the climatological rate. NICAM, FV3, and ICON are very close to the climatological mean in the Sahel, but ICON underestimates and FV3 overestimates precipitation in the TWP. The strong NICAM precipitation on 1 August in the TWP results from the initial shock (see Section 2.1); thereafter,

the total accumulated precipitation in NICAM tracks the top end of the TRMM range.

3.3 Texture of Convection

The "texture" (fine-scale morphology) of precipitation is an illuminating diagnostic of how well models simulate the details of convection and differences between land and ocean regions (Inoue et al., 2008). Figures 3.3 and 3.4 show characteristic snapshots of precipitation in the NFIS models for the Sahel and TWP, respectively. For each model, we have selected the output times with the maximum regional-mean precipitation rate after the two-day spin-up period.

In the Sahel, the NFIS models all produce realistic squall lines with narrow, short-lived bands of precipitation that are characteristic of the region (Figure 3.3) (Redelsperger & Lafore, 1988; Redelsperger et al., 2002). However, FV3 and SAM have an excess of light precipitation that is uncharacteristic of the Sahel (Figure 3.3c, g). Much of this light precipitation comes from shallow cumulus clouds (parameterized in FV3) which are not apparent in the FWP snapshot. The areal extent of thin cirrus clouds in NICAM is much larger than in the other models (Figure 3.3b). In all models, there is a strong collocation between the FWP and precipitation fields in which the precipitation tracks with the cloud field.

Similarly, in the TWP, NICAM, FV3, and SAM reproduce the large, widespread convective systems typically observed over tropical oceans (Figure 3.4) (Bousquet & Chong, 2000). FV3 and SAM again have expansive regions of unrealistically light precipitation, but to a lesser extent than in the Sahel. The precipitation in ICON consists of small pockets of "popcorn" convection scattered throughout the region (Figure 3.4e). As in the Sahel, areas of intense precipitation collocate with higher FWPs. In NICAM, the entire 10°×10° TWP box has frozen water in the atmospheric column (Figure 3.4b). Although there is diversity in the details of precipitation and FWP in individual models that is generally consistent in the Sahel and TWP, the models simulate a reasonable texture of both precipitation and convection and capture the expected regional differences in land and ocean convection.

As with precipitation, the vertical structure of convective clouds is plausibly simulated in

the NFIS models, but with clear inter-model differences. Figures 3.5 (SHL) and 3.6 (TWP) show time series of the vertical cloud structure within a $1^\circ \times 1^\circ$ box during the first 10 days of the model run. These figures highlight the qualitative differences in land and ocean convection (e.g., Liu et al., 2007), which the models capture nicely. Convection in the Sahel (Figure 3.5) is more sporadic and often deeper than that in the TWP, where convection is nearly constant (Figure 3.6). Unexpectedly, the simulated deep convective clouds in the Sahel lack support from low clouds below the melting level in NICAM, FV3, and ICON.

For all models, the 6 hourly precipitation rates and cloud structures are consistent with the precipitation texture in Figures 3.3 and 3.4. The excessive TTL ice is consistent with the pervasive FWP in NICAM in both regions. For ICON in the TWP, the precipitation rates are substantially lower than in the other models, which agrees with the popcorn texture in the FWP and precipitation snapshots. The more intense convection in FV3 in both regions is evident in the depth of convection in Figures 3.5b and 3.6b as well as the higher FWPs within the deep convective cells in Figures 3.3d and 3.4d.

All NFIS models have overshooting convection in the Sahel, which often penetrates past the cold point in NICAM and FV3 (Figure 3.5a, b). As in the average temperature profiles (Figure 3.1a, b), ICON places the cold point tropopause lower in the TTL than NICAM, FV3, or SAM. The cold points within the Sahel $1^\circ \times 1^\circ$ box vary more over time than in the TWP. The frequency of convection reaching past the cold point in the models is surprising because very few precipitation features observed in the tropics extend above the lapse rate tropopause level (Liu & Zipser, 2005).

The typical vertical cloud structure differs between models. NICAM contains significantly more ice in the TTL than in any of the other models (Figure 3.5a). Much of this additional ice comprises anvil or cirrus clouds with a low FWC. For FV3 in the Sahel (Figure 3.5b), convection reaches higher than other models, occasionally penetrating above 18 km. As shown in Figure 3.3c, the squall lines in ICON are followed by a region of lighter precipitation; this feature is apparent in the cloud structure where regions of high LWC indicative of low liquid clouds follow the convective cores near the melting level (Figure 3.5c). SAM is marked

by persistent thick ice clouds with tops extending into the TTL (Figure 3.5d). Some of these clouds are thick anvils detraining off of the convective cores, but others appear detached with little liquid cloud below.

The vertical cloud structure in the TWP generally matches the qualitative texture expected of ocean convection, but with model-specific biases similar to the Sahel. NICAM has relatively little liquid cloud but persistent TTL ice up to 18 km altitude (Figure 3.6a). The ice within the TTL is almost entirely located above or near the tops of deep convective cores, whereas in the Sahel there are more frequent detached cirrus and anvils. ICON has a higher concentration of liquid water to support the ice cloud than in any other model, with supercooled liquid at altitudes as high as 10 km in updrafts (Figure 3.6c). SAM (Figure 3.6d) also has a lot of low liquid cloud beneath the deep convective clouds but has much more FWC than ICON in these columns, as in the Sahel (Figure 3.5d).

3.4 Diurnal Cycle of Precipitation

The timing and amplitude of the 38-day diurnal cycle of precipitation for all models is similar to the TRMM 2006–2016 climatology, especially in the Sahel (Figure 3.7). Simulated Sahel rainfall peaks 2–3 hours too early in the Sahel (Figure 3.7a), but 2–3 hours too late in the TWP (Figure 3.7b). Nevertheless, the explicit deep convection in the DYAMOND GSRMs vastly reduces known biases in the diurnal timing of precipitation over land in GCMs (Bechtold et al., 2004).

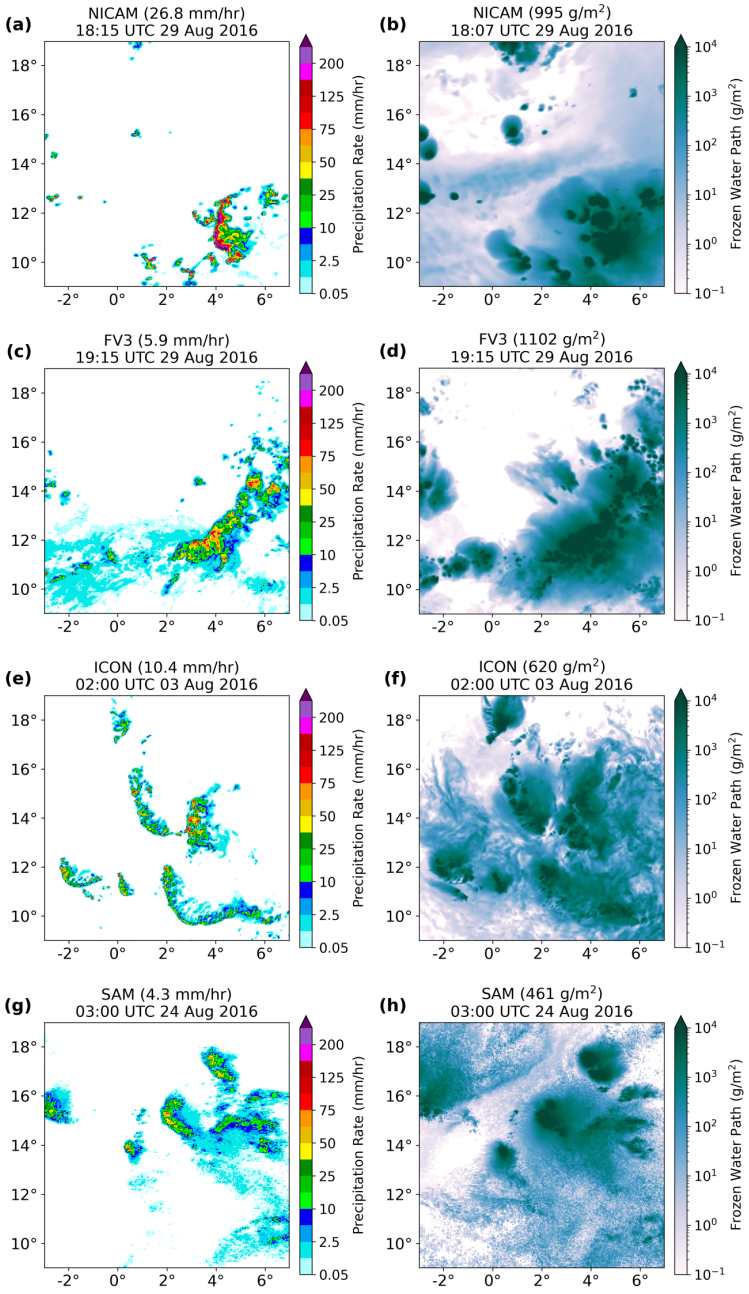

Figure 3.3: Snapshots of (left) precipitation rate and (right) frozen water path (FWP) over the entire $10^\circ \times 10^\circ$ box in the Sahel. Rates below 0.05 mm hr^{-1} and FWPs below 0.1 g m^{-2} are masked. The numbers in each panel title indicate the regional-mean precipitation rate or FWP for each snapshot. The timing of the saved FWP output for NICAM is offset from the precipitation by 7.5 minutes.

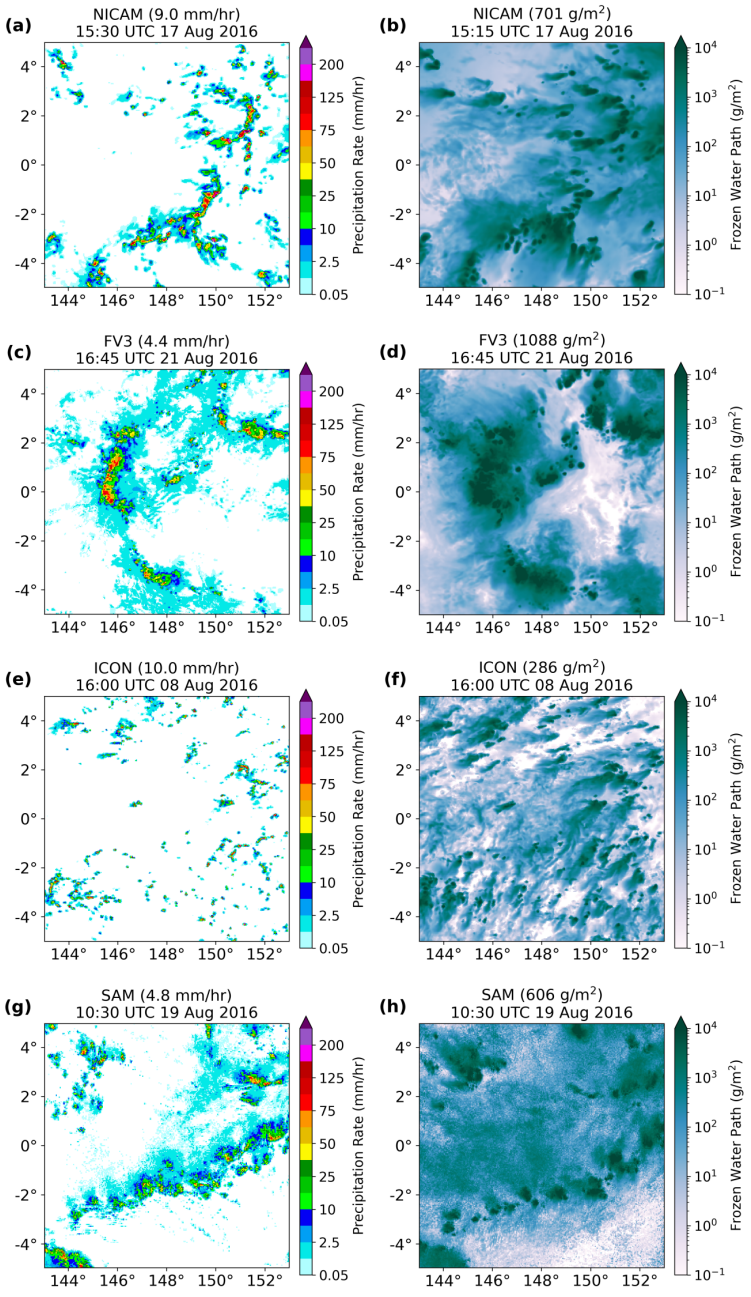

Figure 3.4: As in Figure 3.3, but for the TWP.

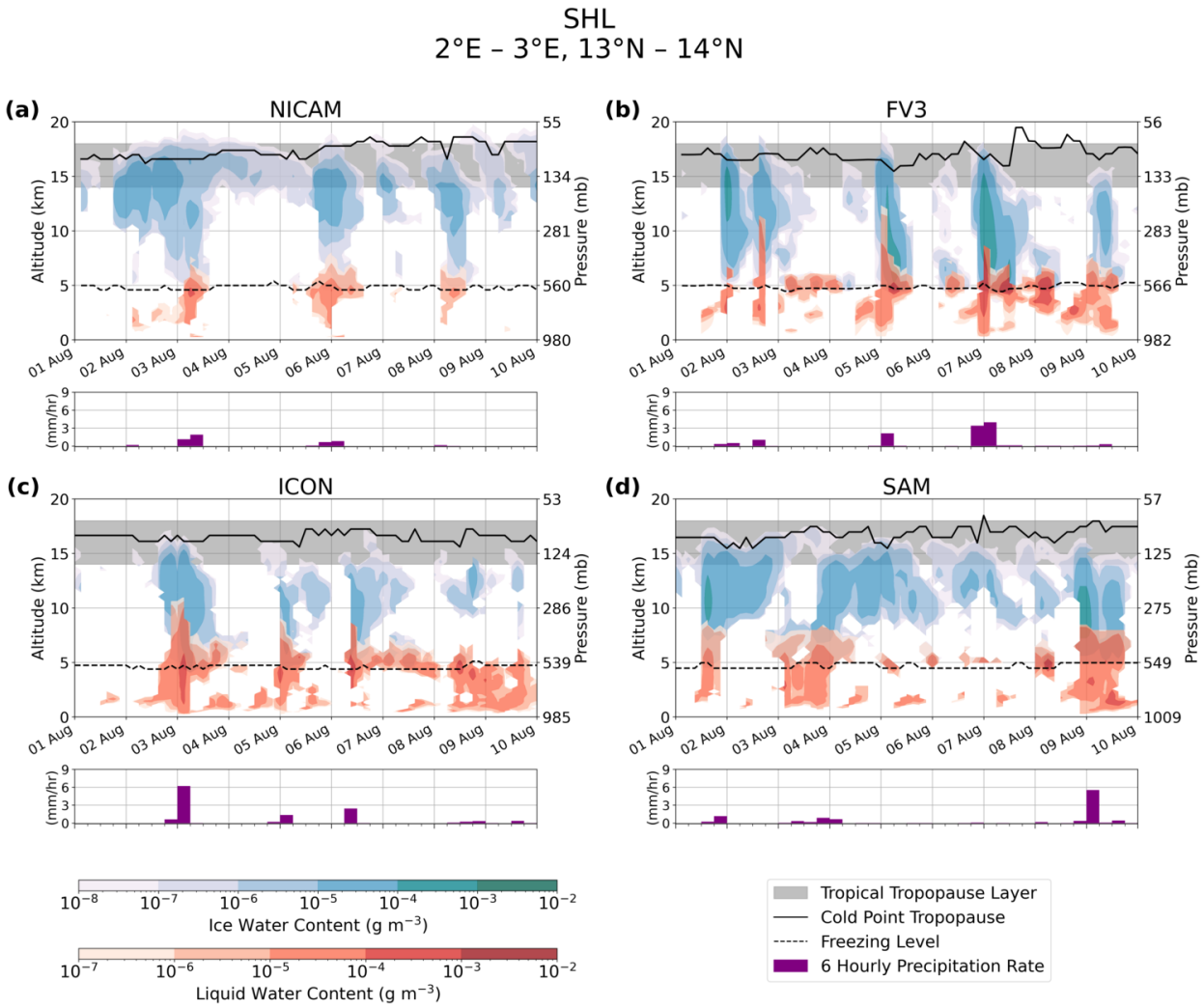

Figure 3.5: Time series of the convective cloud structure for the NFIS models in the Sahel. Ice water content is shaded in blue and liquid water content is shaded in red. Purple bars indicate the 6 hourly precipitation rate. The solid black line shows the cold point tropopause while the dashed black line shows the melting level. The TTL is shaded in grey. Model output is averaged over a $1^\circ \times 1^\circ$ box located at 2°E–3°E, 13°N–14°N, approximately centered over the AMMA site in Niamey, Niger. The first 48 hours (1–2 August) should be regarded as the model spin-up period.

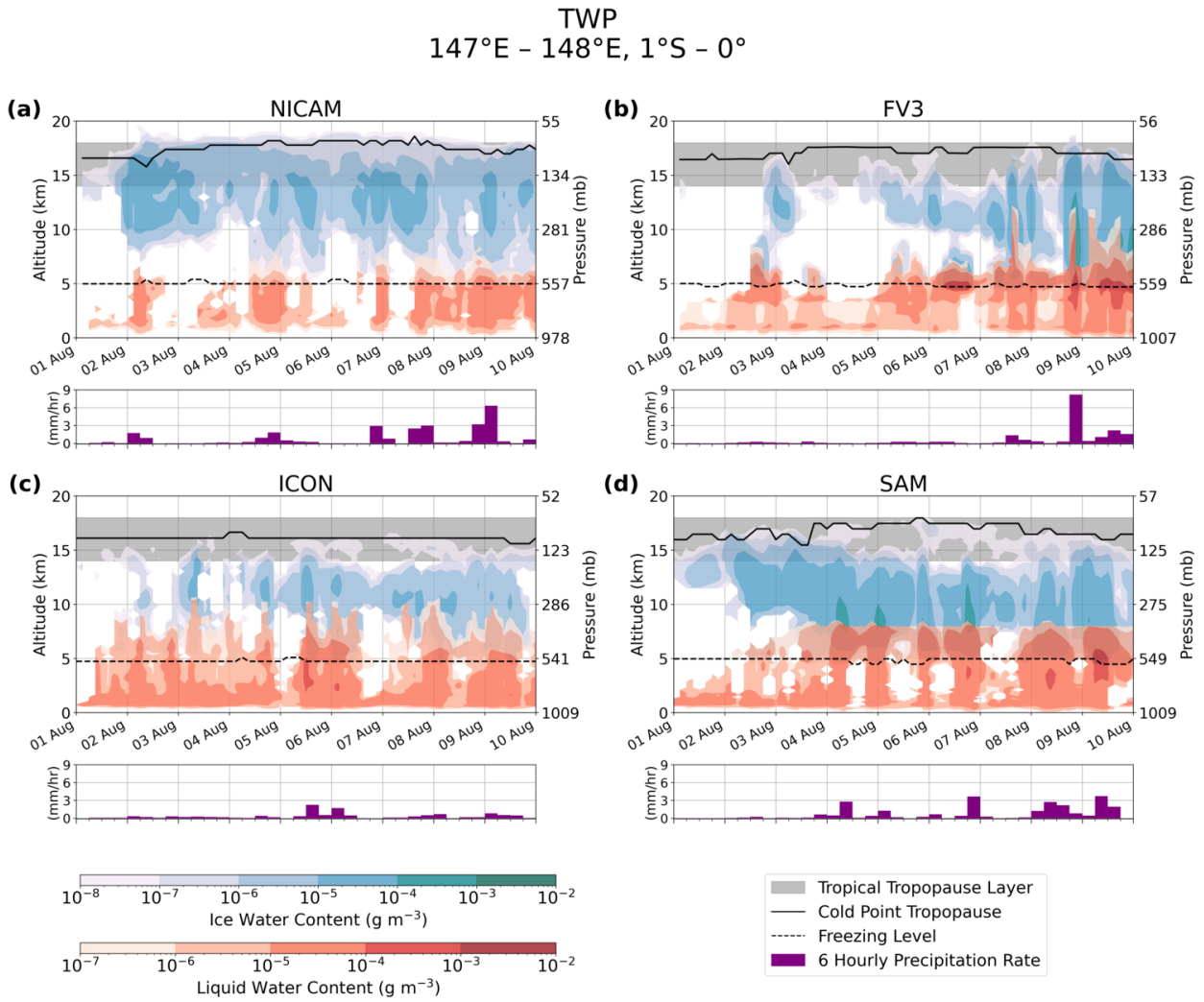

Figure 3.6: As inn Figure 3.5, but for the TWP. Model output is averaged over a $1^\circ \times 1^\circ$ box located at 147°E–148°E, 1°S–0°, approximately centered over the ARM site in Manus, Papua New Guinea. For NICAM, the first 48 hours (1–2 August) were affected by the initial shock in precipitation and should be ignored (see section 2.1).

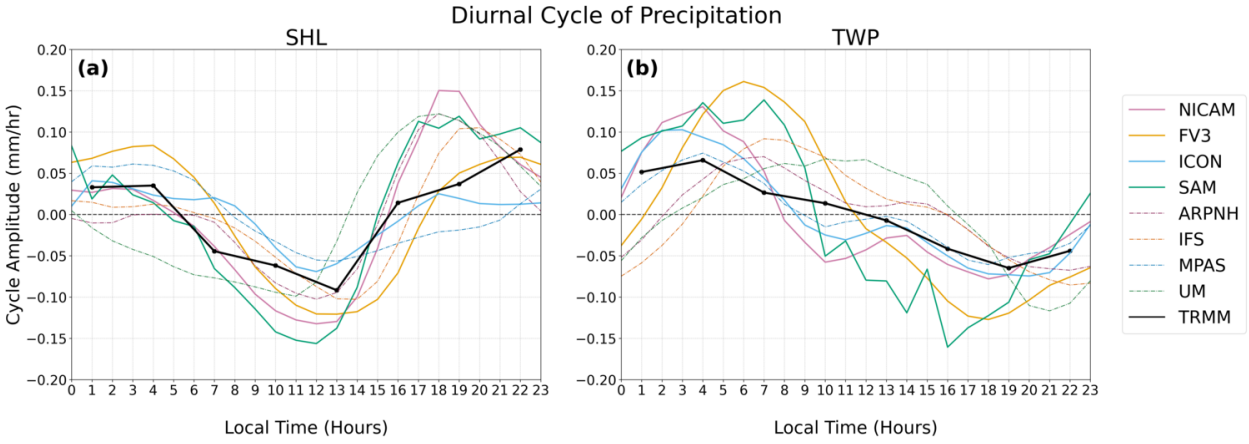

Figure 3.7: Amplitude of the regional-mean diurnal cycle of precipitation in (a) the Sahel and (b) the TWP for all DYAMOND models and for the 2006–2016 TRMM climatology. Precipitation rates are averaged at each hour for days 3–40 of the model run.

Chapter 4

MICROPHYSICS

Next, we examine the differences in the model output of microphysical variables, both within the TTL and integrated over the entire grid column.

4.1 Frozen Water Content and TTL Composition

NICAM is the only DYAMOND model for which we have the 3D graupel and snow output needed to plot their horizontally-averaged profiles. The vertical profiles of ice water content (IWC), IWC + snow water content (SWC), and IWC + SWC + graupel water content (GWC) for NICAM are plotted alongside DARDAR-estimated FWC in Figure 4.1a. Cloud ice dominates in the TTL, while snow and graupel peak at 6–7 km, just above the melting level. NICAM's total FWC peaks around the same level as the observations, but is overestimated. In the TWP, NICAM has much larger FWC on average at all levels than in the Sahel, but the relative levels and magnitudes of IWC, SWC, and GWC have the same trend across regions (see Figure A.1).

Inside the TTL, the main frozen condensate type is cloud ice, which was archived for all four NFIS models. Thus, we compare the model IWC profiles in the TTL to DARDAR. NICAM, FV3, and SAM scatter within a plausible range around the observational estimate between 14–17 km. The FV3 IWC profile is closest to the data, while SAM has lower IWCs and NICAM has slightly higher IWCs. ICON greatly underestimates the observational profile of IWC throughout the entire TTL. For NICAM, the total FWC is slightly larger than the IWC at 14 km, but the contributions of snow and graupel become negligible above $\sim$17 km. It is unclear if adding snow and graupel would make up for the differences in IWC between models seen in Figure 4.1b.

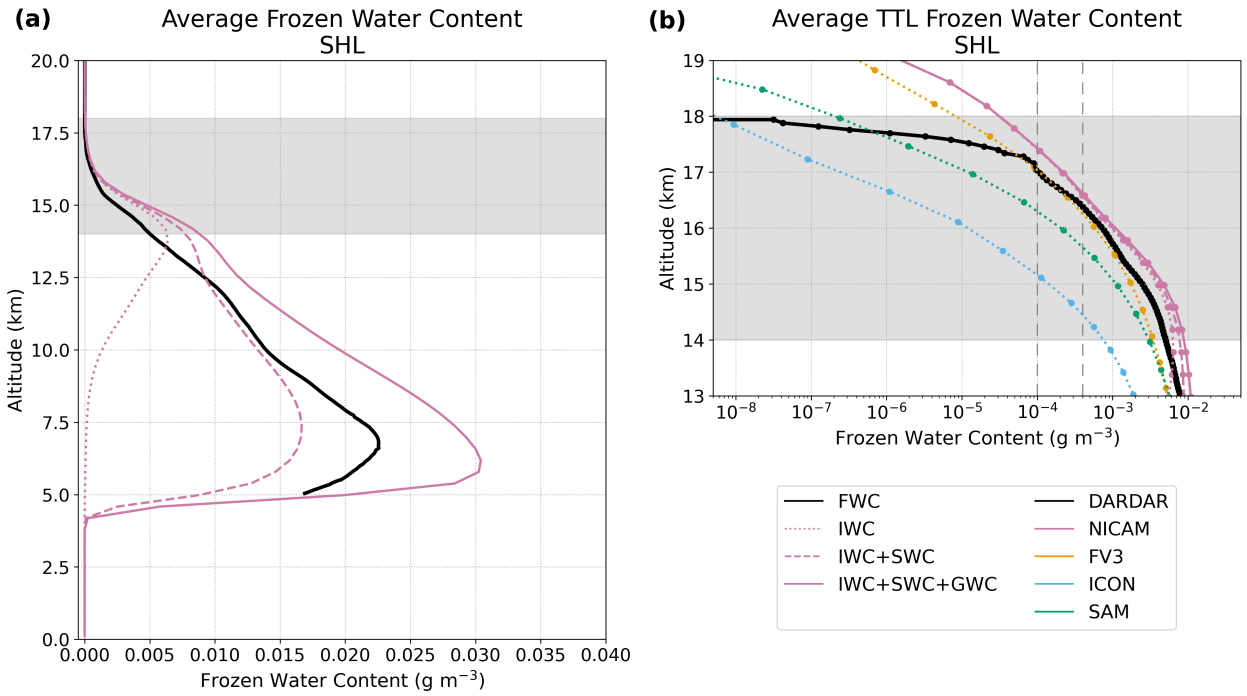

Figure 4.1: Area- and time-mean vertical profiles of frozen water contents (FWCs) in the Sahel. (a) Ice (dotted pink line), ice + snow (dashed pink line), and ice + snow + graupel (solid pink line) water contents for NICAM. The DARDAR FWC profile is shown in black. (b) ice water content (dotted lines) for all NFIS models; ice + snow (dashed pink line) and ice + snow + graupel (solid pink line) water contents for NICAM; and DARDAR FWC (solid black line). Note that the x-axis of panel (b) is logarithmic. The dashed vertical lines indicate the approximate detection limits of the lidar at night (left; 1×10^{-4} g m^{-3}) and during the day (right; 4×10^{-4} g m^{-3}) (Avery et al., 2012).

4.2 Vertically Integrated Water Paths

In addition to IWP, GWP, and SWP, the DYAMOND intercomparison stored the column mass of the rain water path (RWP) and liquid water path (LWP). Figure 4.2 compares the time and regional averages of these quantities in the Sahel to DARDAR (see Figure A.2 for the TWP equivalent). Since hydrometeors affect radiative fluxes, we also compare the time-mean simulated OLR to CERES CCCM data in Figure 4.2. The output for snow, graupel, and rain water paths was not saved for ARPNH or UM, so there is more frozen and liquid

water in those models than shown here. These models are separated from the models with complete information by the vertical dashed lines in Figure 4.2.

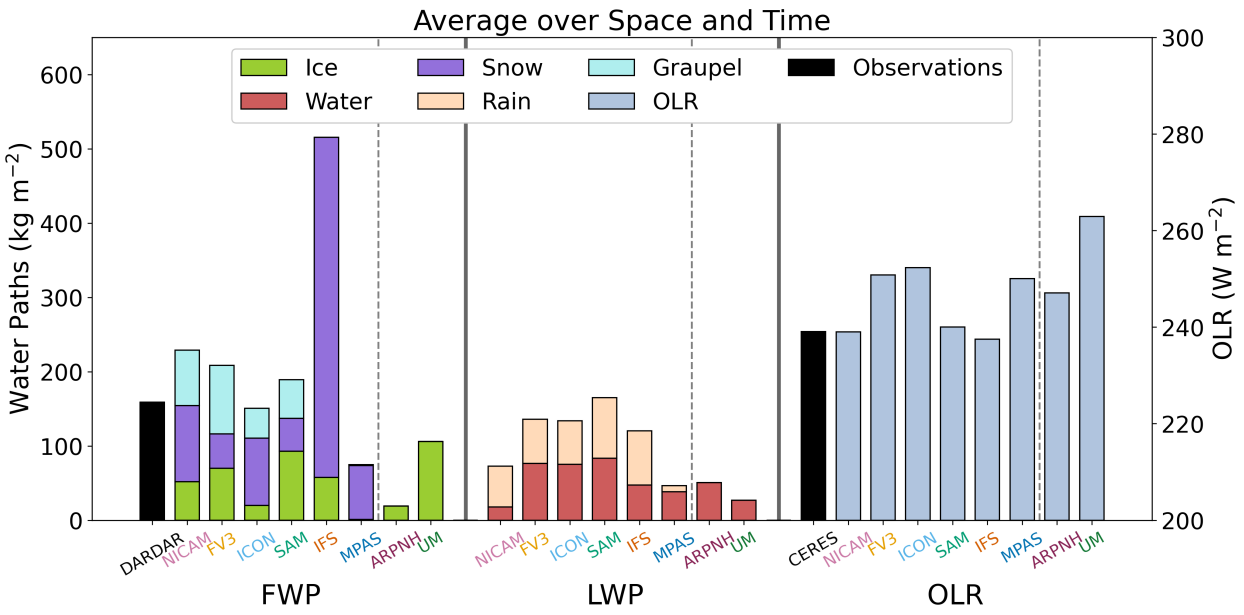

Figure 4.2: Bar chart of the time- and regional-mean frozen water paths (FWPs), liquid water paths (LWPs), and outgoing longwave radiation (OLR) in the Sahel for all DYAMOND models. Black bars indicate observations of FWP from DARDAR and OLR from CERES. The vertical black dashed lines separate the models with complete information from those which did not save all column-integrated water paths. Note that the IFS microphysics scheme does not include graupel.

The left group of bars in Figure 4.2 shows a large inter-model variation in the FWP and its partitioning into frozen hydrometeor types. The FWP in IFS is almost twice that of DARDAR; however, the uncertainty in DARDAR FWP retrievals may be quite large, especially within thick clouds. In NICAM, FV3, ICON, SAM, and MPAS, the FWPs are much closer to the observed value, but the relative amounts of ice, snow, and graupel vary drastically between these models. For example, MPAS has almost no graupel or ice while ice makes up about half of the total FWP in SAM. These differences emphasize the point made in Section 2.1 that the cloud ice alone does not comprise the total FWC in the models

and that the hydrometeors (e.g., snow) may have a different definition in each model.

The center bars in Figure 4.2 compare the condensed water paths, which are more consistent across models. FV3, ICON, and IFS all have nearly identical amounts of cloud liquid and rain water, whereas NICAM and MPAS have much less.

The right bars in Figure 4.2 show a wide inter-model range in the average OLR. The models divide into two groups: those with average OLR close to the CERES observations (NICAM, SAM, and IFS) and those with more OLR than the observations (FV3, ICON, ARPNH, MPAS, and UM). The spread in OLR between these groups is over 25 W m^{-2}, whereas the uncertainty in the CERES OLR is only 3 W m^{-2} (Kato et al., 2018).

The differences in FWPs do not fully account for the OLR variation. It would be reasonable to assume that the models with more OLR have less frozen water than the others on average, but this is not always the case. For example, NICAM and IFS have a much higher FWP than DARDAR and the other models, but their average OLR is still very close to the observed mean. The mean OLR is also affected by model differences in the assumed radiative properties of each hydrometeor type in the microphysics scheme, such as the specification of their effective radii and which types are radiatively active. Additionally, mean OLR varies with the fractional coverage of clouds in each model.

Figure 4.3 compares the cumulative distribution functions (CDFs) of FWP between DARDAR and the DYAMOND models. These CDFs are computed from large FWPs to small ones so that, for example, the value at 10 g m^{-2} indicates the fraction of grid columns with an FWP exceeding 10 g m^{-2}. Since we define cirrus-free columns to be those with FWP < 0.1 g m^{-2} (see Section 2.5), the CDF at 0.1 g m^{-2} is equivalent to the ice cloud fraction. The dependence of simulated FWP distribution on the different hydrometeors is shown with additional lines for the CDFs of IWP and IWP + SWP. The steeper slope approaching 0.1 g m^{-2} indicates that the smaller FWPs are more frequent in the models than in the data. Still, the smallest values of FWP may not be radiatively significant, and thus the thinnest simulated cirrus may not necessarily affect the heating profiles or top-of-atmosphere radiation balance.

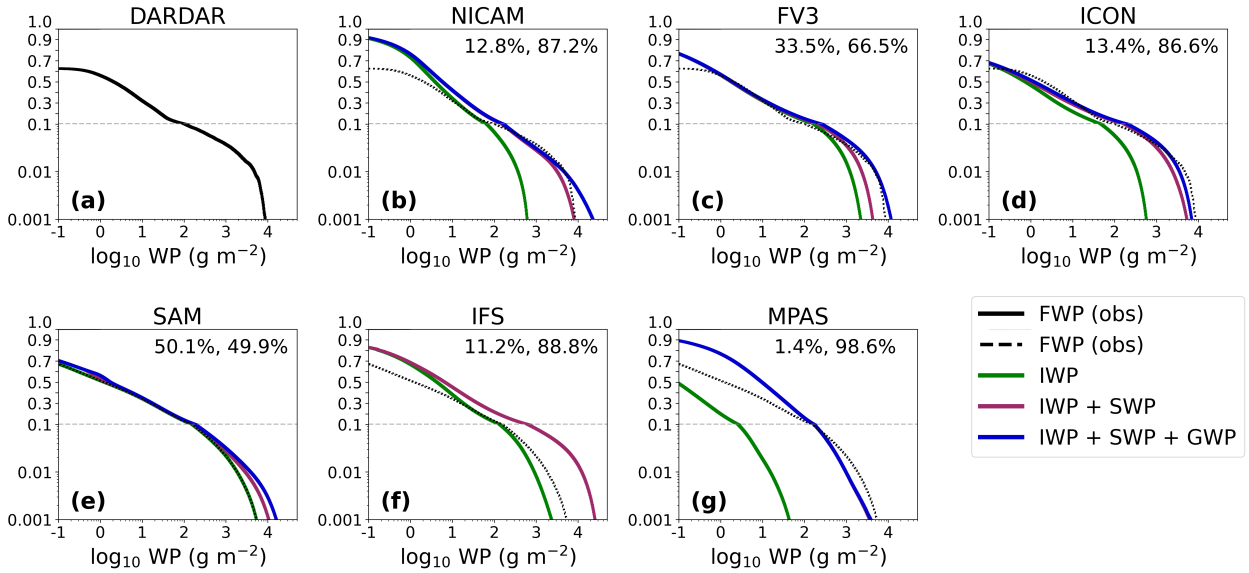

Figure 4.3: Cumulative distribution functions for ice (IWP; green line), ice + snow (IWP + SWP; pink line), and ice + snow + graupel (IWP + SWP + GWP; blue line) water paths for all models in the Sahel compared to DARDAR frozen water path observations (FWP; solid black line in a), dashed in b-g)). Values are accumulated from largest to smallest. ARPNH and UM are omitted because they do not save the 2D output of column-integrated snow or graupel water paths. The y-scale is logarithmic below 0.1 and linear above; the apparent discontinuity at 0.1 is an artifact of this split. The numbers in the upper-right corner of each panel show (left) the percentage of the total FWP from ice and (right) the percentage of total FWP from snow and graupel. These numbers cannot be deduced directly from this figure but are included to emphasize the large contributions of snow and graupel. Again, note that the IFS microphysics scheme does not include graupel.

The addition of SWP and GWP highlights the substantial contribution of snow and graupel to the overall frozen water mass in the DYAMOND models. The percentages in each panel of Figure 4.3b–h list the proportion of frozen mass from ice and snow + graupel, respectively. Ice is the most significant in SAM, constituting about half of the total frozen water mass. In all other models, snow and graupel make up the majority of the frozen mass, from 66.5% in FV3 to 98.6% in MPAS. These differences in partitioning mostly apply to the thickest clouds with high FWPs; the IWP makes up most of the FWP at values below $\sim$10 g m^{-2} for all except MPAS. Likewise, as shown in Figure 4.1, thin cirrus within

the TTL are primarily composed of cloud ice in NICAM. Nevertheless, the large contributions of snow and graupel further stress that we cannot directly compare the simulated cloud ice to the observed frozen water in areas of deep convection.

As mentioned above, the CDFs at 0.1 g m^{-2} represents an ice cloud fraction. All models overestimate the observed ice cloud fraction of ∼0.6, with most falling between ∼0.7 and ∼0.8. NICAM and MPAS have a much larger cloud cover with an ice cloud fraction of 0.9. Qualitatively, the TWP results are similar to the Sahel (see Figure A.3). All but IFS have a larger ice cloud fraction in the TWP than in the observations, but the proportion of frozen mass from snow + graupel falls within a few percent of the Sahel values. NICAM still has the largest ice cloud fraction, which is a surprising 0.999 in the TWP (Figure A.3). Overall, the microphysics schemes in the models produce consistent cloud property biases specific to each model across the tropics.

Chapter 5

TROPICAL TROPOPAUSE LAYER CIRRUS

Finally, we use the NFIS models to try to understand how TTL cirrus are related to convection and what role convective mass fluxes play in the composition of the TTL.

5.1 TTL Cirrus and Convection

The diurnal cycle of convection and the collocation of convection with TTL cirrus are shown in the 40-day time series in Figure 5.1. Only FV3 is shown here for brevity; equivalent figures for NICAM, ICON, and SAM are included in Appendix B (Figures B.1–B.3). The diurnal cycle in the Sahel is much stronger and more distinct than in the TWP as expected (e.g., Yang & Slingo, 2001; Nesbitt & Zipser, 2003). In the Sahel, the deep convection is marked by periodic bouts of very low OLR, higher precipitation rates, and high IWP indicative of deep cumulonimbus towers (Figure 5.1a, c, e). Characteristic of the more persistent, widespread convective storms observed over tropical oceans, the regions of intense precipitation and high IWP occur more frequently and for longer periods of time in the TWP (Figure 5.1b, d, f). The convection and diurnal cycles shown in Figure 5.1 are qualitatively consistent with those for the other models (Figures B.1–B.3) despite the inter-model differences in convection described in Chapter 3.

Peaks in TTL IWP coincide with areas of large total column IWP (Figure 5.1e–h). This suggests that the TTL ice is mostly located over deep convection, which qualitatively agrees with the collocation between total column FWP and precipitation demonstrated in Figures 3.3 and 3.4. In both regions, the NFIS models also have frequent thinning anvils evident in the smaller IWPs extending away from the convective cores, but isolated TTL cirrus are not readily apparent. Therefore, TTL ice is mostly located in the vicinity of convection, with

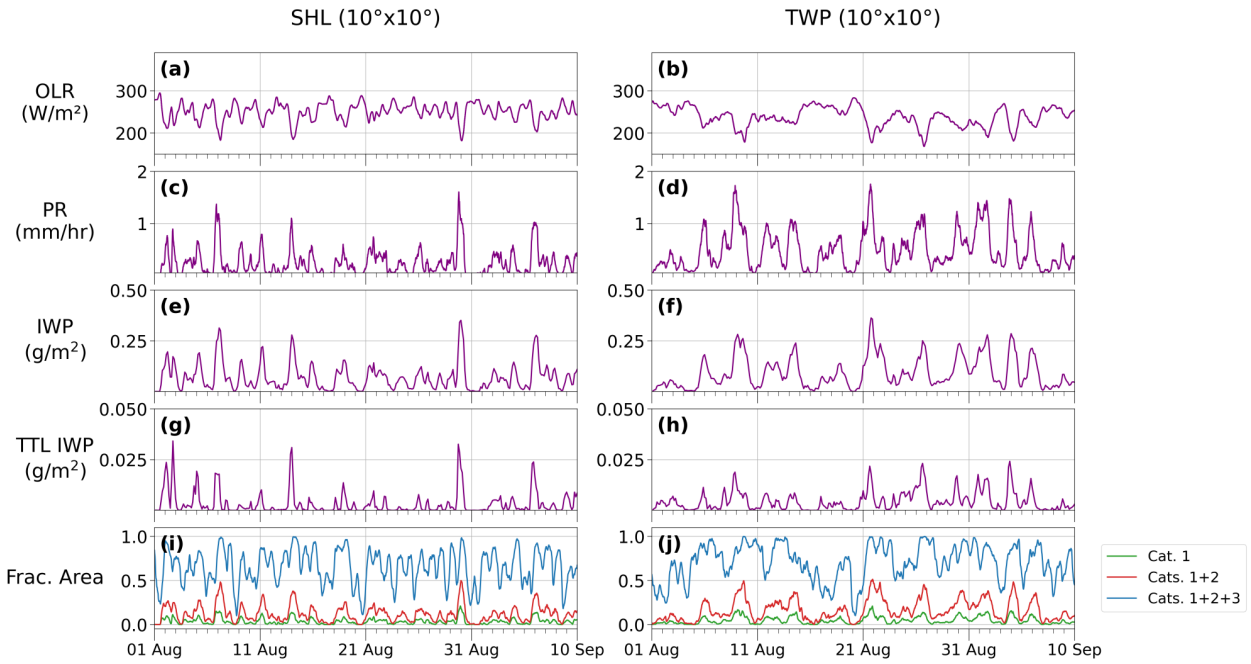

Figure 5.1: Time series for FV3 over days 1–40 of the model run: (a–b) area-mean outgoing longwave radiation (OLR); (c–d) area-mean precipitation rate (PR); (e–f) area-mean total column ice water path (IWP); (g–h) area-mean TTL IWP; and (i–j) fractional area of Category 1, Categories 1–2, and Categories 1–3 columns for FV3 over days 1–40 of the model run. Area-means and fractional areas are computed over the 10°×10° (left) Sahel and (right) TWP regions. For the TTL IWP, ice water content is integrated between the model levels closest to 14 and 18 km, which sometimes lie slightly outside of this range.

the majority of the ice mass concentrated directly over deep convection.

Similarly, the area spanned by anvil cirrus in the 10°×10° regions strongly correlates with that of deep convection (Figure 5.1i–j). Categories 1 and 2 are tightly coupled with each other and with convection in terms of low OLR, high precipitation rate, and large IWPs (Figure 5.1). For FV3, the fractional area of Category 2 lags behind Category 1 by about 3 hours in the Sahel and 5.5 hours in the TWP with a a maximum correlation coefficient of 0.9 in both regions. The coupling between Categories 1 and 2 is qualitatively similar in NICAM, ICON, and SAM (see Figures B.1–B.3). Category 3 thin cirrus track more closely with deep convection and anvils in ICON and SAM while the thin cirrus columns cover

almost the entire 10°×10° area in NICAM. These relationships indicate that most anvils and thick cirrus are likely generated from deep convection, but other physical processes must contribute to generating and maintaining thinner cirrus.

5.2 Injection of Water Vapor and Frozen Water into the TTL

In Figure 5.2a and c, we bin cloud IWC and water vapor content (WV) in Sahel grid cells at 14 km altitude (the nominal base of the TTL) by the collocated vertical velocity for the NFIS models as well as binned mass fluxes for NICAM only. The w bins are subjectively chosen to span the range of simulated updrafts and downdrafts; the probability distribution functions (PDFs) of vertical velocity are shown in Figure 5.2b. Figure 5.2a also shows the total FWC (i.e., including snow and graupel) for NICAM, the only model for which these variables were stored. The graupel and snow water contents may be substantial (up to 10 times larger than IWC) in areas of deep convection with strong updrafts and downdrafts. Thus, graupel and snow may dominate the vertical advective fluxes of frozen water into the TTL, so we only compare the w-binned vertical mass fluxes of frozen water and water vapor for NICAM (Figure 5.2).

The cloud IWC at 14 km varies greatly between models, but the relative differences across w bins are qualitatively consistent (Figure 5.2a). The IWC in FV3, ICON, and SAM increases by about three orders of magnitude from the weakest to the strongest updrafts and downdrafts, which occur within deep convective clouds. The increase in IWC across bins is not as drastic in the NICAM because its IWC is larger in the weakest w bins. For all models, the IWC is relatively symmetric between the largest positive and negative bins, suggesting that cloud ice is typically circulated between nearby convective updrafts and downdrafts. Despite the differences in the model simulation of land and ocean convection discussed in Section 3, the trends in IWC at different updraft and downdraft speeds are remarkably similar between regions (see Figure A.4a).

Although the 14 km WV varies much less across w bins than the IWC, the trends differ somewhat between models (Figure 5.2c). For example, WV in SAM is nearly constant with

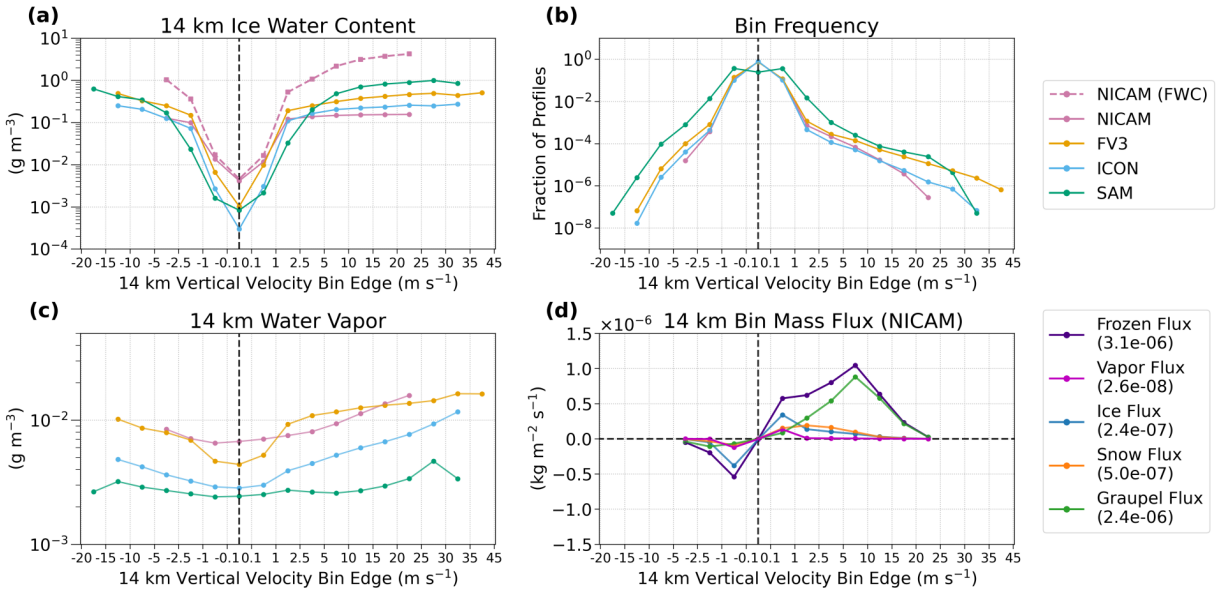

Figure 5.2: Selected variables sampled at all 14 km grid points for days 3–40 in the Sahel and averaged over vertical velocity bins: (a) cloud ice water content (pink dashed line shows NICAM frozen water content); (b) bin frequency; (c) water vapor; and (d) frozen water vapor, water vapor, ice, snow, and graupel mass fluxes for NICAM only.

w, but WV in FV3 and ICON increases with updraft speeds. Nevertheless, the 14 km WV values are strikingly consistent; for each model and each w bin, all WV values lie within one order of magnitude from each other. As with IWC, the trends in WV are consistent across the tropics in the NFIS models (Figure A.4c).

The general shape of the vertical velocity PDF is consistent between the NFIS models, but there is inter-model spread in the infrequent extreme values (Figure 5.2b). Except for SAM, the models agree that in 99.9% of the grid cells, w lies within the -1 to 1 m s^{-1} bins; this is expected given the intermittency of deep convection that penetrates into the TTL. SAM simulates more 14 km updrafts and downdrafts of intermediate strength (1–10 m s^{-1}) than other models. SAM also produces downdrafts up to -20 m s^{-1} while NICAM does not simulate any downdrafts below -5 m^{-1} in either region. The strongest convective updrafts reach 45 m s^{-1} in FV3, which is 10–20 m s^{-1} larger than in the other models. The overall

shape of the vertical velocity PDF is the same in the TWP as in the Sahel, but there is even more disagreement among the strongest updrafts and downdrafts (Figure A.4b). Although ICON and NICAM both have stronger maximum 14 km updraft speeds in the Sahel, the updrafts do not seem to be systematically stronger over land for FV3 or SAM. Overall, these differences in extreme values reflect diverse formulations of both model dynamics and microphysics that bear further scrutiny.

Figure 5.2d shows the mass fluxes at 14 km of water vapor and frozen water for NICAM only. The frozen mass flux is further broken down into the cloud ice, snow, and graupel fluxes. Because the WV is relatively constant across w bins (Figure 5.2c), the w-partitioning of 14 km water vapor flux is qualitatively similar to that of dry air and can be used as a proxy for the total air motion. The bin-averaged vapor flux in NICAM is largest in the $\pm$0.1–1 m s^{-1} bins and negligible everywhere else (Figure 5.2d, dark pink line). In contrast, the frozen mass flux distribution (Figure 5.2d, purple line) is weighted toward updrafts exceeding 1 m s^{-1} because they contain much more frozen water than nearly quiescent air. In all bins, the frozen mass flux is much larger than the water vapor flux, consistent with the observationally-based estimates of Bolot and Fueglistaler (2021). Similarly, the integrated mass flux values given in the lower legends of Figures 5.2 and A.4 show that in both regions, the upward frozen mass flux in NICAM at 14 km is much larger than the vapor mass flux and is the principal source of water in the TTL. Ice sedimentation is not considered in the distributions in Figures 5.2d and A.4d. We presume that the ice sedimentation quickly offsets much of this upward flux, but we still expect that some injected frozen water remains and spreads into extensive TTL cirrus or ultimately sublimates and moistens the TTL (see Figure 3.1c, d).

Among the frozen hydrometeor fluxes (Figure 5.2d) in NICAM, cloud ice dominates in the $\pm$0.1 m s^{-1} bins that represent the vast majority of the grid points over time (Figure 5.2b). In the 1 to 15 m s^{-1} bins, snow and cloud ice fluxes make up a small but nearly equal proportion of the total frozen mass flux. At updrafts stronger than 5 m s^{-1}, however, the graupel flux constitutes nearly all of the frozen mass flux. In the TWP, there is less upward

frozen mass flux overall. The graupel flux makes up a much smaller component of the total bin-integrated frozen water flux, but still exceeds the cloud ice and snow fluxes for updrafts stronger than 5 m s^{-1} (see Figure A.4d).

5.3 Categorization of Water Injection by Frozen Water Path

Partitioning the mass fluxes into the three FWP categories described in Section 2.5 further reveals the importance of deep convection in transporting water into the TTL, even outside of columns with strong updrafts. Table 5.1 (see Table A.1 for the TWP equivalent) contains the frequencies of occurrence of each category as well as the category-conditional frequencies of vertical velocities above ± 2.5 m s^{-1} and category-conditional average mass fluxes. Category 1 is the least frequent, containing 3.4% or less of all columns in the Sahel. Category 1 is slightly more common in the TWP for all models except ICON (Table A.1), which is consistent with the more frequent convection over the oceans. There is a large inter-model spread in the Category 2 and 3 values and consequently in the amount of clear sky. We expect most columns to fall into Category 3 because the TTL is dominated by very thin cirrus (e.g., Sassen et al., 2009); this is true in the Sahel, but Category 2 occurs most often in NICAM and SAM in the TWP. As shown in the vertical velocity PDFs (Figure 5.2b), the overwhelming majority of vertical motion in the TTL is very weak, even in areas of deep convection. Vertical velocities exceed ± 2.5 m s^{-1} in only 0.2% of Category 1 columns in SAM and less than 0.024% of Category 1 columns in NICAM, FV3, and ICON (Table 5.1). The strong upward mass fluxes are therefore not restricted to the Category 1 columns that have strong updraft speeds.

The category-conditional average mass fluxes show the differences in roles played by each hydrometeor within the different physical processes in the TTL. Category 1 accounts for the majority of the total frozen mass flux in both regions even though it contains a small fraction of columns. As with the integrated values, most of the average Category 1 frozen mass flux comes from graupel flux in NICAM. Graupel flux is slightly less important in the TWP, but still accounts for about half of the average frozen flux (Table A.1). In Category 2, however,

Table 5.1: Results from the frozen water path categorization. Columns list frequency of each frozen water path category, percentage of columns in each category where $|w| \geq 2.5$ m s^{-1}, and regional- and time-mean mass fluxes for the NFIS models in the Sahel. The mass fluxes are weighted by category frequency.

Model	Cat.	Freq.	Freq. of $\lvert w\rvert \geq 2.5$ m s^{-1}	Avg. vapor flux (kg m^{-2} s^{-1})	Avg. frozen flux (kg m^{-2} s^{-1})	Avg. ice flux (kg m^{-2} s^{-1})	Avg. snow flux (kg m^{-2} s^{-1})	Avg. graupel flux (kg m^{-2} s^{-1})
NICAM	1	3.1 %	0.011 %	7.3×10^{-10}	3.1×10^{-6}	2.6×10^{-7}	4.9×10^{-7}	2.4×10^{-6}
	2	38.8 %	0.018 %	6.3×10^{-11}	-1.2×10^{-8}	-1.9×10^{-8}	6.8×10^{-9}	5.9×10^{-10}
	3	50.0 %	0.002 %	2.8×10^{-9}	1.9×10^{-10}	8.8×10^{-11}	1.0×10^{-10}	1.2×10^{-14}
FV3	1	3.4 %	0.024 %	5.0×10^{-8}		1.3×10^{-6}		
	2	21.4 %	0.033 %	-1.1×10^{-8}		1.9×10^{-8}		
	3	39.4 %	0.004 %	5.7×10^{-9}		1.8×10^{-9}		
ICON	1	3.2 %	0.010 %	3.7×10^{-9}		2.4×10^{-7}		
	2	20.3 %	0.011 %	-2.9×10^{-9}		6.3×10^{-9}		
	3	26.5 %	0.001 %	2.1×10^{-9}		4.6×10^{-10}		
SAM	1	3.4 %	0.200 %	1.1×10^{-8}		2.9×10^{-6}		
	2	32.1 %	0.025 %	4.1×10^{-9}		1.4×10^{-7}		
	3	35.2 %	0.003 %	2.1×10^{-8}		1.1×10^{-8}		

most of the frozen flux comes from cloud ice flux. Both the average frozen and cloud ice fluxes are negative, but this does not indicate a net downward flux; these fluxes integrate to nearly zero in Category 2. The average vapor flux in Category 2 is also much larger than in Category 1, particularly in the TWP (Table A.1), but is still dwarfed by the frozen mass flux. Unsurprisingly, the average frozen mass flux is very small in Category 3 since the thin cirrus contain very little frozen water. Instead, the vapor flux is about 10 times larger than the frozen mass flux within Category 3 and nearly 4 times larger than the Category 1 vapor flux in both regions (Tables 5.1 and A.1).

When the mass fluxes in Categories 2 and 3 are binned by w as with the total-column fluxes in Figure 5.2d, the distributions do not reach large w values and are approximately symmetric around 0 (not shown). This symmetry suggests that in areas of both anvil and thin cirrus, the mass fluxes indicate a recycling of air through the 14 km level instead of a systematic upward flux. By extension, this indicates that there is likely much less

sedimentation in these areas compared to deep convection. Altogether, the relationships between mass fluxes and FWP categories are surprisingly similar between the Sahel and TWP despite the differences in the characteristics of simulated land and ocean convection described in Chapter 3.

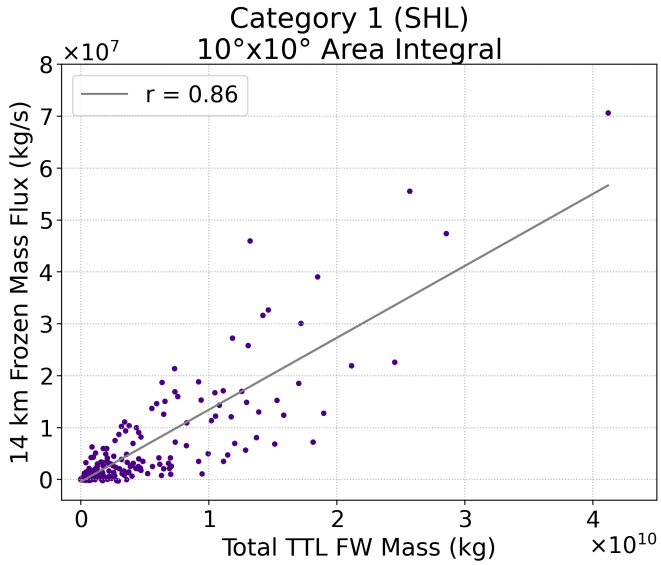

Figure 5.3: Correlations between the area-integrated Category 1 frozen mass flux at 14 km and the total mass of frozen water (FW) in the TTL in Category 1 for NICAM in the Sahel. Each point represents one instantaneous time step over days 3–40 of the model run with variables integrated over the 10°×10° Sahel region. The least-squares regression line is shown in grey with the correlation coefficient (r) in the legend.

Within Category 1, the 10°×10° area-integrated frozen mass flux in NICAM at each time step is strongly correlated with the instantaneous mass of frozen water within the TTL (Figure 5.3). The frozen mass flux is only weakly related to the total spatial area spanned by Category 1 columns at each time step, with a correlation coefficient half as large as that in Figure 5.3 (0.42 vs. 0.86). Therefore, a larger area of deep convection does not necessarily bring more frozen water into the TTL. The relationship in Figure 5.3 suggests that there is a regional-mean time scale of about 722 seconds (the reciprocal of the slope of the regression line) in the Sahel for the frozen water injected into the TTL to fall out or evolve into thinner

cirrus (i.e., Categories 2 and 3). The same relationship is present in the TWP, but the time scale is longer at 1575 seconds (see Figure A.5). Compared to the Sahel, the weaker updrafts in the TWP tend to loft smaller ice particles that will take longer to sediment out of the TTL. Since NICAM has much more cloud ice in the TTL in both regions than FV3, ICON, or SAM, it is unclear if this ice removal timescale will quantitatively hold for the other models.

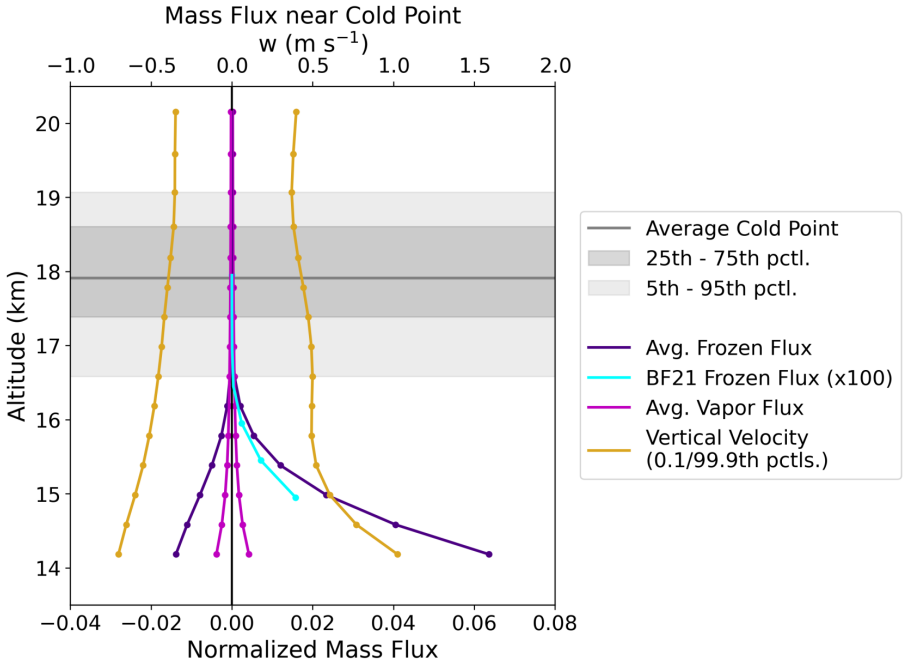

Figure 5.4: Vertical profiles of normalized frozen water (purple lines) and vapor mass fluxes (dark pink lines) for NICAM in the Sahel as well as the normalized estimates of frozen mass flux from Bolot and Fueglistaler (2021) times 100 (BF21; cyan lines). The mass fluxes for NICAM are split between updrafts and downdrafts, averaged over the 10°×10° region and time, and weighted by the relative frequency of the updrafts or downdrafts. The gold lines show the 0.1th and 99.9th percentiles of vertical velocity. The average cold point height is shown in the solid grey line while the 5th–95th (25th–75th) percentiles are shaded in light (dark) grey. All percentiles are taken over the 10°×10° Sahel region and days 3–40 of the model run.

In NICAM, deep convection injects frozen water and vapor at 14 km and deposits it throughout the depth of the TTL. Figure 5.4 shows vertical profiles of the average frozen water and vapor mass fluxes (normalized by the 38-day average precipitation rate in the

Sahel) as well as the largest 0.1% of vertical velocities within the updrafts or downdrafts (see Figure A.6 for the TWP equivalent, normalized by the TWP average precipitation rate). These profiles are for all columns, but as previously discussed, the Category 1 frozen mass flux makes up nearly all of the total frozen mass flux. In both regions, the frozen mass flux dominates throughout the lower TTL up to about 16.5 km, at which point it is overtaken by the vapor flux. This patterns agrees qualitatively with Bolot and Fueglistaler (2021), who found that deep convection is more important for moisture transport below the cold point at ∼16–17 km than large-scale advection (i.e., our Category 3 mass fluxes). However, the frozen mass flux values in NICAM are larger by a factor of ∼100 in both regions than the observationally-based, tropics-wide estimates from Bolot and Fueglistaler (2021). We normalize the estimates of ice flux from Figure 3 in Bolot and Fueglistaler (2021) by the area of their 30°S–30°N domain as well as the 38-day average Sahel or TWP precipitation rate. These estimates are then plotted alongside the NICAM values in Figures 5.4 and A.6.

5.4 Frozen Water Flux into the TTL in Other Models

We cannot generalize the mass flux results in NICAM to the other models. The regional- and time-mean cloud ice mass fluxes at 14 km vary by a factor of 10 in the NFIS models within both regions (Table 5.1). We also expect the specific values of 14 km frozen and vapor mass fluxes to differ significantly between the NFIS models based on the vertical velocities, FWC, and WV. Although the 14 km IWC is very similar between models in the bins above ± 5 m s^{-1} (Figure 5.2a), there are substantial differences in the relative proportions of cloud ice, snow, and graupel (Figure 4.3). Thus, the 14 km FWC will likely vary more than the 14 km IWC. Likewise, FV3 and ICON both have very different frequencies of updrafts stronger than 10 m s^{-1} than NICAM (Figure 5.2), which determine the most intense mass flux values in those models.

Regardless of the anticipated differences in the amounts of mass injected into the TTL, we still expect deep convection to be the most important process in supplying water into the TTL. In all of the NFIS models, the concentration of cloud ice over deep convection

is very high (see Section 5.1). This proportion will only increase once graupel and snow are considered because these hydrometeors make up 50–87% of the total integrated FWP in FV3, ICON, and SAM (Figure 4.3). Since the 14 km WV in FV3, ICON, and SAM is similar to that in NICAM (Figure 5.2c), we can assume that the frozen mass flux will be much larger than the vapor flux in the other models. Nevertheless, we cannot draw any definitive conclusions about the frozen mass flux in other models without access to the 3D profiles of snow and graupel in FV3, ICON, or SAM.

Chapter 6

CONCLUSIONS

6.1 Summary and Discussion

In this study, we have used satellite and reanalysis data to evaluate the simulation of convectively generated cirrus in GSRMs from the DYAMOND project. These GSRMs all have horizontal grid spacing below 5 km, which permits explicit convection (Stevens et al., 2019). We focused on four models which archived cloud ice at the full native grid resolution: NICAM, FV3, ICON, and SAM. We analyzed two representative 10°×10° latitude-longitude regions, one over the Sahel in western Africa and one over the tropical West Pacific Ocean.

Before analyzing how convection generates tropical cirrus in the DYAMOND GSRMs, we first assessed how well the GSRMs reproduce deep convection. As a group, the DYAMOND GSRMs simulate deep convective precipitation, its organization, and its diurnal cycle fairly well over both the land and ocean regions, though inter-model scatter is large. In contrast, GCMs struggle with these tasks. The GSRM-simulated convective updraft and downdraft strengths have qualitatively similar frequency distributions. All the GSRMs produce frequent overshooting convection that reaches the TTL; in most models, convective updrafts occasionally penetrate the cold point tropopause. In all GSRMs, the time-mean relative humidity with respect to ice is ∼70–90% in the TTL in both regions.

For the convective cloud properties (water content vertical profiles and the cloud microphysics, including partitioning between cloud liquid, ice, snow, and graupel) and the convective injection of frozen water into the TTL, differences between GSRMs exceed differences between land and ocean regions. In all models and in both regions, the most intense convective updrafts inject nearly all of the incoming frozen water into the TTL. We presume that most of this injected ice sediments out of the TTL near the deep convection, although

we did not have the necessary information to be sure. We found that across the models, the mass of frozen water within the TTL correlates with the deep convective frozen mass flux into the TTL; their ratio suggests an ice residence time of about ten to thirty minutes.

Our analysis was limited by the output variables available for most of the DYAMOND GSRMs. Having the 3D profiles of snow and graupel water contents would allow for evaluation of inter-model differences in the frozen mass fluxes and TTL FWC. Because cloud microphysics parameterizations are a major source of inter-model differences, saving the full hydrometeor profiles should be prioritized in future GSRM simulations.

We have focused on how water vapor and frozen water reach the TTL. What happens to the injected mass afterward is also critical to understanding the relationship between TTL cirrus and deep convection, e. g.. how quickly air moves from Category 1 (deep convection) to Category 2 (thick cirrus) and how much frozen water is transported between categories vs. how much sediments out.

Despite their present limitations, GSRMs are a promising complement to climate models for the simulation of cirrus initiated by deep convection, including within the TTL. This study shows that sub-grid processes drive the substantial variation between models. Specifically, the model microphysics and, to a lesser extent, the dynamical flow solver may both be important. We suspect that improved microphysics would more readily advance the simulation of tropical cirrus than higher spatial resolutions. The sub-5 km horizontal and 200–500 m vertical grid spacings seem sufficient to simulate cirrus and may capture gravity wave activity around deep convection that is thought to be important for TTL cirrus, though this has not been clearly shown. Radiatively-driven circulations within TTL cirrus (Durran et al., 2009) would require finer grids to explicitly resolve; whether sub-grid turbulence parameterizations can represent this process adequately remains to be seen. Overall, this work has demonstrated that GSRMs model deep convection realistically enough to form a good foundation for simulating convectively generated cirrus and their impacts on the TTL, climate more broadly, and climate change. Careful observationally-based improvements of GSRMs are needed to fully realize this potential.

6.2 Future Work

The recently completed second phase of the DYAMOND initiative brought together another set of GSRMs to simulate the boreal winter from 20 January to 1 March, 2020 (Klocke et al., 2019). Some of these new GSRM simulations have saved output not available in the first phase, such as the full 3D profiles of snow and graupel. This additional output will enable us to study the mass flux of frozen water into the TTL in multiple models. Using the new set of DYAMOND simulations, we will expand the analysis presented in this thesis to consider additional tropical land regions such as South America or south-central Africa, which both have frequent overshooting convection during the boreal winter (Zipser et al., 2006).

We intend to use the new GSRM simulations to address the question of how much water injected by deep convection remains in the TTL long enough to influence its moisture content. By computing the ice sedimentation flux in the GSRMs, we can close the mass budget between convective injection into the TTL, sedimentation out of the TTL, and horizontal transport (between adjacent columns and between FWP categories) to estimate a more precise residence time of injected frozen water than that suggested by Figures 5.3 and A.5. We will also extend the analysis above the TTL in order to study the mixing between the upper tropopause and lower stratosphere that occurs within areas of deep convection in the models. Our ultimate goal is to assess the relative importance of overshooting deep convection in hydrating the lower stratosphere.

BIBLIOGRAPHY

Arteta, J., Marecal, V., & Riviere, E. D. (2009). Regional modelling of tracer transport by tropical convection – Part 1: Sensitivity to convection parameterization. *Atmos. Chem. Phys.*, 20.

Avery, M., Winker, D., Heymsfield, A., Vaughan, M., Young, S., Hu, Y., & Trepte, C. (2012). Cloud ice water content retrieved from the CALIOP space-based lidar: CALIOP ICE WATER CONTENT. *Geophysical Research Letters*, *39*(5). doi: 10.1029/2011GL050545

Bechtold, P., Chaboureau, J.-P., Beljaars, A., Betts, A., Köhler, M., Miller, M., & Redelsperger, J.-L. (2004). The simulation of the diurnal cycle of convective precipitation over land in a global model. *Quarterly Journal of the Royal Meteorological Society*, *130*(604), 3119–3137. doi: 10.1256/qj.03.103

Berthou, S., Rowell, D. P., Kendon, E. J., Roberts, M. J., Stratton, R. A., Crook, J. A., & Wilcox, C. (2019). Improved climatological precipitation characteristics over West Africa at convection-permitting scales. *Climate Dynamics*, *53*(3-4), 1991–2011. doi: 10.1007/s00382-019-04759-4

Bolot, M., & Fueglistaler, S. (2021). Tropical Water Fluxes Dominated by Deep Convection Up to Near Tropopause Levels. *Geophysical Research Letters*, *48*(4). doi: 10.1029/2020GL091471

Bousquet, O., & Chong, M. (2000). The oceanic mesoscale convective system and associated mesovortex observed 12 December 1992 during TOGA-COARE. *Quarterly Journal of the Royal Meteorological Society*, *126*(562), 189–211. doi: 10.1002/qj.49712656210

Chao, W. C. (2013). Catastrophe-Concept-Based Cumulus Parameterization: Correction of Systematic Errors in the Precipitation Diurnal Cycle over Land in a GCM. *Journal of*

the Atmospheric Sciences, *70*(11), 3599–3614. doi: 10.1175/JAS-D-13-022.1

Delanoë, J., & Hogan, R. J. (2008). A variational scheme for retrieving ice cloud properties from combined radar, lidar, and infrared radiometer. *Journal of Geophysical Research*, *113*(D7), D07204. doi: 10.1029/2007JD009000

Delanoë, J., & Hogan, R. J. (2010). Combined CloudSat-CALIPSO-MODIS retrievals of the properties of ice clouds. *Journal of Geophysical Research*, *115*, D00H29. doi: 10.1029/2009JD012346

Deng, M., Mace, G. G., Wang, Z., & Lawson, R. P. (2013). Evaluation of Several A-Train Ice Cloud Retrieval Products with In Situ Measurements Collected during the SPARTICUS Campaign. *Journal of Applied Meteorology and Climatology*, *52*(4), 1014–1030. doi: 10.1175/JAMC-D-12-054.1

Dessler, A. E., Palm, S. P., Hart, W. D., & Spinhirne, J. D. (2006). Tropopause-level thin cirrus coverage revealed by ICESat/Geoscience Laser Altimeter System. *Journal of Geophysical Research*, *111*(D8), D08203. doi: 10.1029/2005JD006586

Duda, J. D., & Gallus, W. A. (2013). The Impact of Large-Scale Forcing on Skill of Simulated Convective Initiation and Upscale Evolution with Convection-Allowing Grid Spacings in the WRF*. *Weather and Forecasting*, *28*(4), 994–1018. doi: 10.1175/WAF-D-13-00005.1

Durran, D. R., Dinh, T., Ammerman, M., & Ackerman, T. (2009). The Mesoscale Dynamics of Thin Tropical Tropopause Cirrus. *Journal of the Atmospheric Sciences*, *66*(9), 2859–2873. doi: 10.1175/2009JAS3046.1

Fierli, F., Orlandi, E., Law, K. S., Cagnazzo, C., Cairo, F., Schiller, C., ... Volk, C. M. (2011). Impact of deep convection in the tropical tropopause layer in West Africa: in-situ observations and mesoscale modelling. *Atmospheric Chemistry and Physics*, *11*(1), 201–214. doi: 10.5194/acp-11-201-2011

Fueglistaler, S., Dessler, A. E., Dunkerton, T. J., Folkins, I., Fu, Q., & Mote, P. W. (2009). Tropical tropopause layer. *Reviews of Geophysics*, *47*(1). (Publisher: John Wiley & Sons, Ltd) doi: 10.1029/2008RG000267

Futyan, J. M., Russell, J. E., & Harries, J. E. (2004). Cloud Radiative Forcing in Pacific, African, and Atlantic Tropical Convective Regions. *JOURNAL OF CLIMATE*, *17*, 11.

Haladay, T., & Stephens, G. (2009). Characteristics of tropical thin cirrus clouds deduced from joint CloudSat and CALIPSO observations. *Journal of Geophysical Research*, *114*, D00A25. doi: 10.1029/2008JD010675

Hersbach, H., Bell, B., Berrisford, P., Hirahara, S., Horányi, A., Muñoz-Sabater, J., ... Thépaut, J. (2020). The ERA5 global reanalysis. *Quarterly Journal of the Royal Meteorological Society*, *146*(730), 1999–2049. doi: 10.1002/qj.3803

Huffman, G. J., Adler, R. F., Bolvin, D. T., & Nelkin, E. J. (2010). The TRMM Multi-Satellite Precipitation Analysis (TMPA). In M. Gebremichael & F. Hossain (Eds.), *Satellite Rainfall Applications for Surface Hydrology* (pp. 3–22). Dordrecht: Springer Netherlands. doi: 10.1007/978-90-481-2915-7_1

Huffman, G. J., & Bolvin, D. T. (2018). *TRMM and Other Data Precipitation Set Documentation.* NASA/GSFC. Retrieved 2021-02-19, from `https://docserver.gesdisc.eosdis.nasa.gov/public/project/GPM/3B42_3B43_doc_V7.pdf`

Huffman, G. J., Bolvin, D. T., Nelkin, E. J., Wolff, D. B., Adler, R. F., Gu, G., ... Stocker, E. F. (2007). The TRMM Multisatellite Precipitation Analysis (TMPA): Quasi-Global, Multiyear, Combined-Sensor Precipitation Estimates at Fine Scales. *Journal of Hydrometeorology*, *8*(1), 38–55. doi: 10.1175/JHM560.1

Inoue, T., Satoh, M., Miura, H., & Mapes, B. (2008). Characteristics of Cloud Size of Deep Convection Simulated by a Global Cloud Resolving Model over the Western Tropical Pacific. *Journal of the Meteorological Society of Japan*, *86A*, 1–15. doi: 10.2151/jmsj.86A.1

Jensen, E. J., Toon, O. B., Pfister, L., & Selkirk, H. B. (1996a). Dehydration of the upper troposphere and lower stratosphere by subvisible cirrus clouds near the tropical tropopause. *Geophysical Research Letters*, *23*(8), 825–828. (Publisher: John Wiley & Sons, Ltd) doi: 10.1029/96GL00722

Jensen, E. J., Toon, O. B., Selkirk, H. B., Spinhirne, J. D., & Schoeberl, M. R. (1996b). On the formation and persistence of subvisible cirrus clouds near the tropical tropopause. *Journal of Geophysical Research: Atmospheres*, *101*(D16), 21361–21375. doi: 10.1029/95JD03575

Jensen, E. J., Ueyama, R., Pfister, L., Bui, T. V., Alexander, M. J., Podglajen, A., ... Schoeberl, M. R. (2016). High-frequency gravity waves and homogeneous ice nucleation in tropical tropopause layer cirrus: WAVES AND ICE NUCLEATION. *Geophysical Research Letters*, *43*(12), 6629–6635. doi: 10.1002/2016GL069426

Kato, S., Rose, F. G., Rutan, D. A., Thorsen, T. J., Loeb, N. G., Doelling, D. R., ... Ham, S.-H. (2018). Surface Irradiances of Edition 4.0 Clouds and the Earth's Radiant Energy System (CERES) Energy Balanced and Filled (EBAF) Data Product. *Journal of Climate*, *31*(11), 4501–4527. doi: 10.1175/JCLI-D-17-0523.1

Kato, S., Rose, F. G., Sun-Mack, S., Miller, W. F., Chen, Y., Rutan, D. A., ... Collins, W. D. (2011). Improvements of top-of-atmosphere and surface irradiance computations with CALIPSO-, CloudSat-, and MODIS-derived cloud and aerosol properties. *Journal of Geophysical Research*, *116*(D19), D19209. doi: 10.1029/2011JD016050

Kato, S., Sun-Mack, S., Miller, W. F., Rose, F. G., Chen, Y., Minnis, P., & Wielicki, B. A. (2010). Relationships among cloud occurrence frequency, overlap, and effective thickness derived from CALIPSO and CloudSat merged cloud vertical profiles. *Journal of Geophysical Research*, *115*, D00H28. doi: 10.1029/2009JD012277

Khairoutdinov, M., Randall, D., & DeMott, C. (2005). Simulations of the Atmospheric General Circulation Using a Cloud-Resolving Model as a Superparameterization of Physical Processes. *Journal of the Atmospheric Sciences*, *62*(7), 2136–2154. doi: 10.1175/JAS3453.1

Klocke, D., Miyakawa, T., Satoh, M., Stevens, B., Judt, F., Putman, W., ... Biercamp, J. (2019). *PROJECT DYAMOND 2nd PHASE - THE WINTER.* `https://www.esiwace.eu/services/dyamond/dyamond-2nd-phase-the-winter-experimental-protocol`. (Accessed 3 June 2021)

Krämer, M., Rolf, C., Luebke, A., Afchine, A., Spelten, N., Costa, A., ... Avallone, L. (2016). A microphysics guide to cirrus clouds – Part 1: Cirrus types. *Atmospheric Chemistry and Physics*, *16*(5), 3463–3483. doi: 10.5194/acp-16-3463-2016

Lee, J., Yang, P., Dessler, A. E., Gao, B.-C., & Platnick, S. (2009). Distribution and Radiative Forcing of Tropical Thin Cirrus Clouds. *Journal of the Atmospheric Sciences*, *66*(12), 3721–3731. doi: 10.1175/2009JAS3183.1

Liu, C., & Zipser, E. J. (2005). Global distribution of convection penetrating the tropical tropopause. *Journal of Geophysical Research*, *110*(D23), D23104. doi: 10.1029/2005JD006063

Liu, C., Zipser, E. J., & Nesbitt, S. W. (2007). Global Distribution of Tropical Deep Convection: Different Perspectives from TRMM Infrared and Radar Data. *Journal of Climate*, *20*(3), 489–503. doi: 10.1175/JCLI4023.1

Long, C. N., Mather, J. H., & Ackerman, T. P. (2016). The ARM Tropical Western Pacific (TWP) Sites. *Meteorological Monographs*, *57*, 7.1–7.14. doi: 10.1175/AMSMONOGRAPHS-D-15-0024.1

Luo, Z., & Rossow, W. B. (2004). Characterizing Tropical Cirrus Life Cycle, Evolution, and Interaction with Upper-Tropospheric Water Vapor Using Lagrangian Trajectory Analysis of Satellite Observations. *Journal of Climate*, *17*(23), 4541–4563. doi: 10.1175/3222.1

Mace, G. G., Deng, M., Soden, B., & Zipser, E. (2006). Association of Tropical Cirrus in the 10–15-km Layer with Deep Convective Sources: An Observational Study Combining Millimeter Radar Data and Satellite-Derived Trajectories. *Journal of the Atmospheric Sciences*, *63*(2), 480–503. doi: 10.1175/JAS3627.1

Massie, S., Gettelman, A., Randel, W., & Baumgardner, D. (2002). Distribution of tropical cirrus in relation to convection: DISTRIBUTION OF TROPICAL CIRRUS. *Journal of Geophysical Research: Atmospheres*, *107*(D21), AAC 19–1–AAC 19–16. doi: 10.1029/2001JD001293

Murphy, D. M., & Koop, T. (2005). Review of the vapour pressures of ice and supercooled

water for atmospheric applications. *Quarterly Journal of the Royal Meteorological Society*, *131*(608), 1539–1565. doi: 10.1256/qj.04.94

Nesbitt, S. W., & Zipser, E. J. (2003). The Diurnal Cycle of Rainfall and Convective Intensity according to Three Years of TRMM Measurements. *JOURNAL OF CLIMATE*, *16*, 20.

Putman, W. (2020, August). [Email]. Private communication.

Redelsperger, J.-L., Diongue, A., Diedhiou, A., Ceron, J.-P., Diop, M., Gueremy, J.-F., & Lafore, J.-P. (2002). Multi-scale description of a Sahelian synoptic weather system representative of the West African monsoon. *Quarterly Journal of the Royal Meteorological Society*, *128*(582), 1229–1257. doi: 10.1256/003590002320373274

Redelsperger, J.-L., & Lafore, J.-P. (1988). A Three-Dimensional Simulation of a Tropical Squall Line: Convective Organization and Thermodynamic Vertical Transport. *Journal of Atmospheric Sciences*, *45*(8), 1334 – 1356. (Place: Boston MA, USA Publisher: American Meteorological Society) doi: 10.1175/1520-0469(1988)045⟨1334:ATDSOA⟩2.0.CO;2

Sassen, K., Wang, Z., & Liu, D. (2009). Cirrus clouds and deep convection in the tropics: Insights from CALIPSO and CloudSat. *Journal of Geophysical Research*, *114*, D00H06. doi: 10.1029/2009JD011916

Schoeberl, M. R., Jensen, E. J., Pfister, L., Ueyama, R., Avery, M., & Dessler, A. E. (2018). Convective Hydration of the Upper Troposphere and Lower Stratosphere. *Journal of Geophysical Research: Atmospheres*, *123*(9), 4583–4593. doi: 10.1029/2018JD028286

Slingo, A., Bharmal, N. A., Robinson, G. J., Settle, J. J., Allan, R. P., White, H. E., ... Miller, M. (2008). Overview of observations from the RADAGAST experiment in Niamey, Niger: Meteorology and thermodynamic variables. *Journal of Geophysical Research*, *113*, D00E01. doi: 10.1029/2008JD009909

Sokol, A. B., & Hartmann, D. L. (2020). Tropical Anvil Clouds: Radiative Driving Toward a Preferred State. *Journal of Geophysical Research: Atmospheres*, *125*(21). doi: 10.1029/2020JD033107

Solomon, S., Rosenlof, K. H., Portmann, R. W., Daniel, J. S., Davis, S. M., Sanford, T. J., & Plattner, G.-K. (2010). Contributions of Stratospheric Water Vapor to Decadal Changes in the Rate of Global Warming. *Science*, *327*(5970), 1219–1223. doi: 10.1126/science.1182488

Stephens, G. L., Vane, D. G., Boain, R. J., Mace, G. G., Sassen, K., Wang, Z., ... the CloudSat Science Team (2002). THE CLOUDSAT MISSION AND THE A-TRAIN: A New Dimension of Space-Based Observations of Clouds and Precipitation. *Bulletin of the American Meteorological Society*, *83*(12), 1771–1790. doi: 10.1175/BAMS-83-12-1771

Stevens, B., Satoh, M., Auger, L., Biercamp, J., Bretherton, C. S., Chen, X., ... Zhou, L. (2019). DYAMOND: the DYnamics of the Atmospheric general circulation Modeled On Non-hydrostatic Domains. *Progress in Earth and Planetary Science*, *6*(1), 61. doi: 10.1186/s40645-019-0304-z

Ueyama, R., Jensen, E. J., & Pfister, L. (2018). Convective Influence on the Humidity and Clouds in the Tropical Tropopause Layer During Boreal Summer. *Journal of Geophysical Research: Atmospheres*. doi: 10.1029/2018JD028674

Virts, K. S., & Houze, R. A. (2015). Clouds and Water Vapor in the Tropical Tropopause Transition Layer over Mesoscale Convective Systems. *Journal of the Atmospheric Sciences*, *72*(12), 4739–4753. doi: 10.1175/JAS-D-15-0122.1

Yang, G.-Y., & Slingo, J. (2001). The Diurnal Cycle in the Tropics. *MONTHLY WEATHER REVIEW*, *129*, 18.

Zipser, E. J., Cecil, D. J., Liu, C., Nesbitt, S. W., & Yorty, D. P. (2006). WHERE ARE THE MOST INTENSE THUNDERSTORMS ON EARTH? *Bulletin of the American Meteorological Society*, *87*(8), 1057–1072. doi: 10.1175/BAMS-87-8-1057

Appendix A

ADDITIONAL FIGURES FOR THE TWP

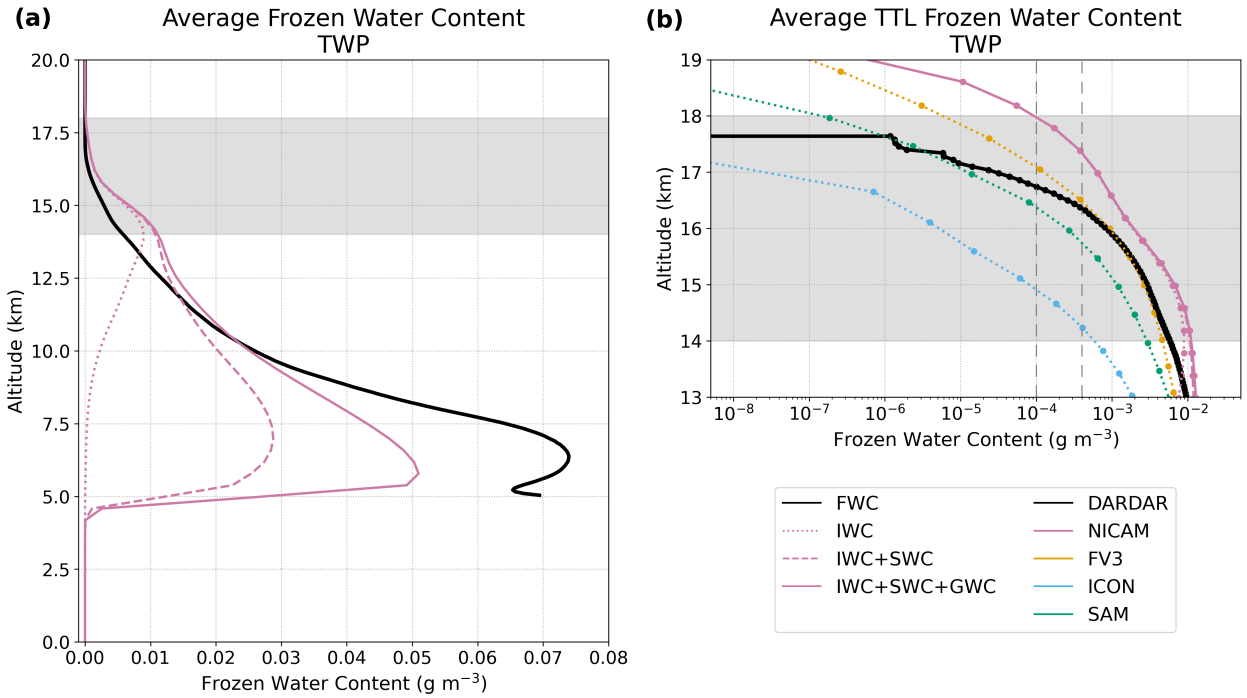

Figure A.1: Equivalent to Figure 4.1, but for the TWP. Area- and time-mean vertical profiles of frozen water contents (FWCs) in the TWP. (a) Ice (dotted pink line), ice + snow (dashed pink line), and ice + snow + graupel (solid pink line) water contents for NICAM. The DARDAR FWC profile is shown in black. (b) ice water content (dotted lines) for all NFIS models; ice + snow (dashed pink line) and ice + snow + graupel (solid pink line) water contents for NICAM; and DARDAR FWC (solid black line). Note that the x-axis of panel (b) is logarithmic. The dashed vertical lines indicate the approximate detection limits of the lidar at night (left; 1×10^{-4} g m^{-3}) and during the day (right; 4×10^{-4} g m^{-3}) (Avery et al., 2012). Note that the TWP region experienced anomalously high precipitation in 2009 when DARDAR measurements were taken, so the apparent underestimation of peak FWC in NICAM is likely exaggerated here.

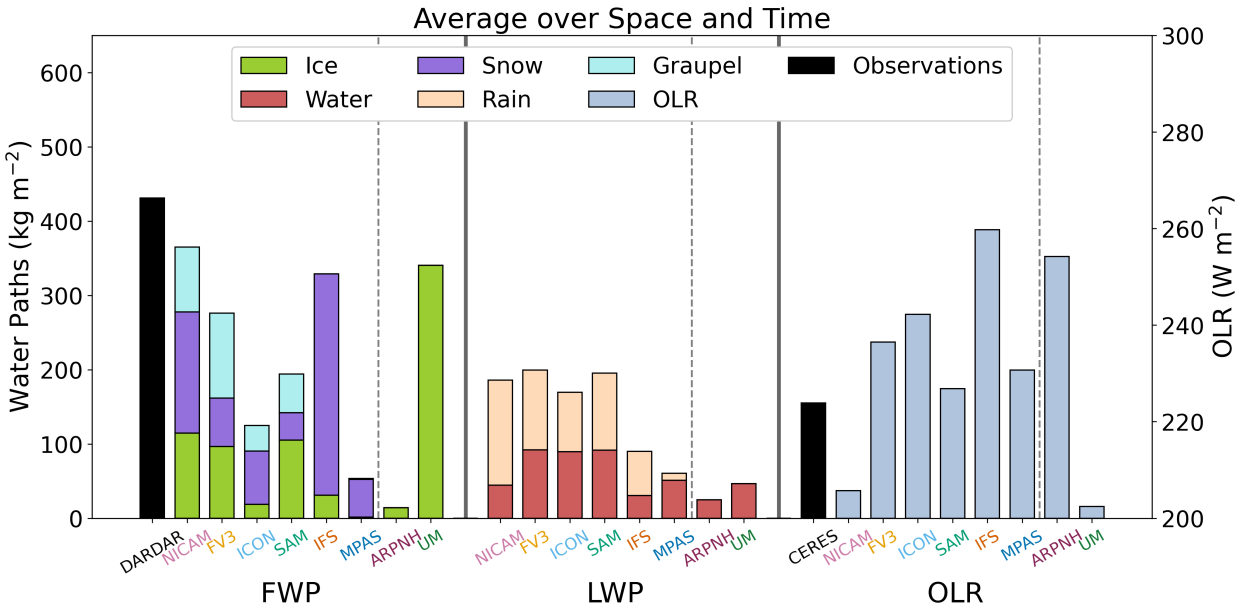

Figure A.2: Equivalent to Figure 4.2, but for the TWP. Bar chart of the time- and regional-mean frozen water paths (FWPs), liquid water paths (LWPs), and outgoing longwave radiation (OLR) in the TWP for all DYAMOND models. Black bars indicate observations of FWP from DARDAR and OLR from CERES. The vertical black dashed lines separate the models with complete information from those which did not save all column-integrated water paths. Note that the IFS microphysics scheme does not include graupel.

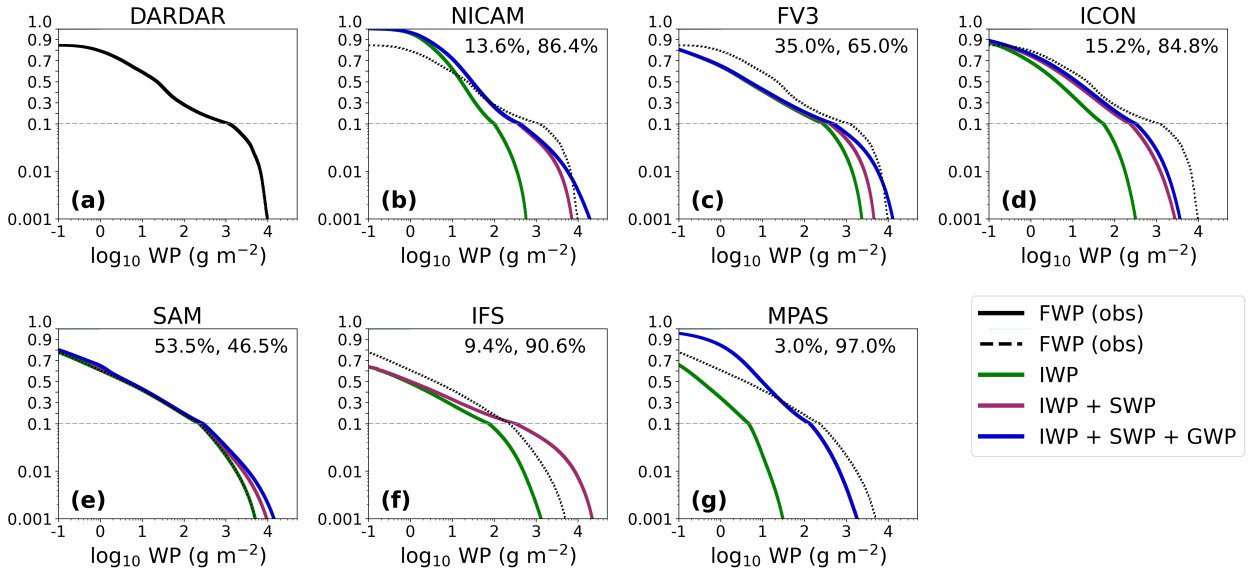

Figure A.3: Equivalent to Figure 4.3, but for the TWP. Cumulative distribution functions for ice (IWP; green line), ice + snow (IWP + SWP; pink line), and ice + snow + graupel (IWP + SWP + GWP; blue line) water paths for all models in the TWP compared to DARDAR frozen water path observations (FWP; solid black line in a), dashed in b-g)). Values are accumulated from largest to smallest. ARPNH and UM are omitted because they do not save the 2D output of column-integrated snow or graupel water paths. The y-scale is logarithmic below 0.1 and linear above; the apparent discontinuity at 0.1 is an artifact of this split. The numbers in the upper-right corner of each panel show (left) the percentage of the total FWP from ice and (right) the percentage of total FWP from snow and graupel. These numbers cannot be deduced directly from this figure but are included to emphasize the large contributions of snow and graupel. Again, note that the IFS microphysics scheme does not include graupel.

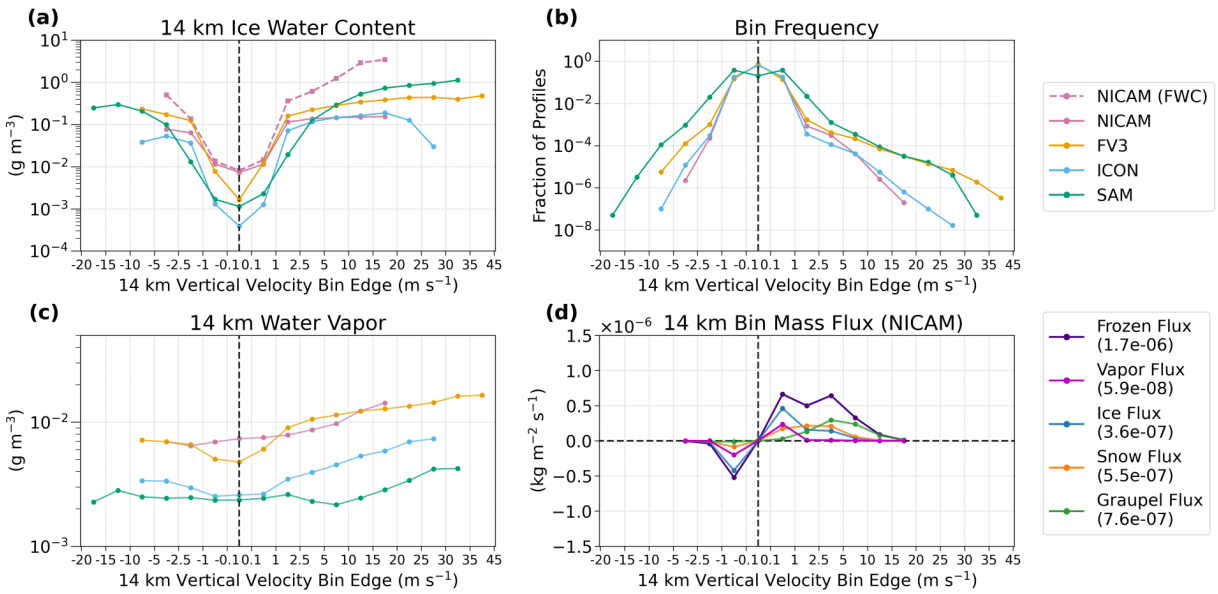

Figure A.4: Equivalent to Figure 5.2, but for the TWP. Selected variables sampled at all 14 km grid points for days 3–40 in the TWP and averaged over vertical velocity bins: (a) cloud ice water content (pink dashed line shows NICAM frozen water content); (b) bin frequency; (c) water vapor; and (d) frozen water vapor, water vapor, ice, snow, and graupel mass fluxes for NICAM only.

Table A.1: Equivalent to Table 5.1, but for the TWP. Results from the frozen water path categorization. Columns list frequency of each frozen water path category, percentage of columns in each category where $|w| \geq 2.5$ m s^{-1}, and regional- and time-mean mass fluxes for the NFIS models in the TWP. The mass fluxes are weighted by category frequency.

Model	Cat.	Freq.	Freq. of $\lvert w\rvert \geq 2.5$ m s^{-1}	Avg. vapor flux (kg m^{-2} s^{-1})	Avg. frozen flux (kg m^{-2} s^{-1})	Avg. ice flux (kg m^{-2} s^{-1})	Avg. snow flux (kg m^{-2} s^{-1})	Avg. graupel flux (kg m^{-2} s^{-1})
NICAM	1	5.4 %	0.010 %	7.1×10^{-8}	1.6×10^{-4}	3.2×10^{-5}	5.4×10^{-5}	7.6×10^{-5}
	2	66.4 %	0.022 %	4.9×10^{-7}	5.5×10^{-6}	3.9×10^{-6}	1.5×10^{-5}	4.5×10^{-9}
	3	28.1 %	0.003 %	3.2×10^{-7}	5.0×10^{-8}	3.9×10^{-8}	1.1×10^{-8}	2.2×10^{-14}
FV3	1	4.8 %	0.039 %	7.3×10^{-6}		1.8×10^{-4}		
	2	29.2 %	0.039 %	1.4×10^{-6}		6.6×10^{-6}		
	3	37.2 %	0.007 %	1.1×10^{-6}		3.1×10^{-7}		
ICON	1	2.8 %	0.001 %	1.4×10^{-7}		1.1×10^{-5}		
	2	32.1 %	0.009 %	-3.9×10^{-7}		9.5×10^{-7}		
	3	33.5 %	0.005 %	4.8×10^{-7}		4.7×10^{-8}		
SAM	1	3.7 %	0.213 %	9.9×10^{-7}		2.3×10^{-4}		
	2	39.5 %	0.055 %	5.8×10^{-7}		1.9×10^{-5}		
	3	37.0 %	0.008 %	2.8×10^{-6}		1.5×10^{-6}		

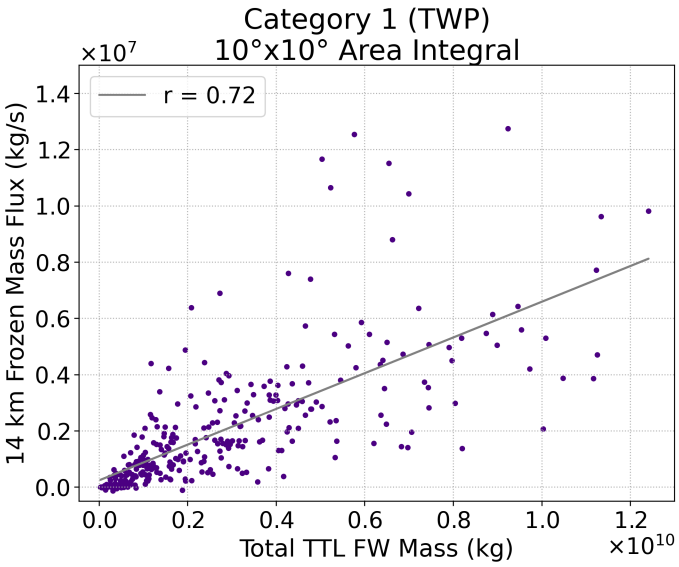

Figure A.5: Equivalent to Figure 5.3, but for the TWP. Correlations between the area-integrated Category 1 frozen mass flux at 14 km and the total mass of frozen water (FW) in the TTL in Category 1 for NICAM in the TWP. Each point represents one instantaneous time step over days 3–40 of the model run with variables integrated over the 10°×10° TWP region. The least-squares regression line is shown in grey with the correlation coefficient (r) in the legend.

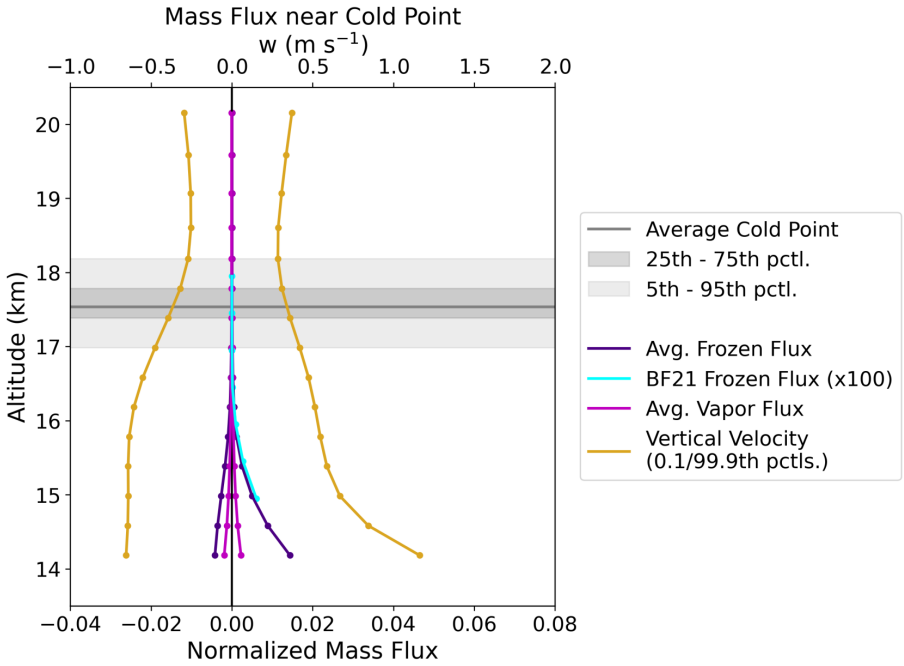

Figure A.6: Equivalent to Figure 5.4, but for the TWP. Vertical profiles of normalized frozen water (purple lines) and vapor mass fluxes (dark pink lines) for NICAM in the TWP as well as the normalized estimates of frozen mass flux from Bolot and Fueglistaler (2021) times 100 (BF21; cyan lines). The mass fluxes for NICAM are split between updrafts and downdrafts, averaged over the 10°×10° region and time, and weighted by the relative frequency of the updrafts or downdrafts. The gold lines show the 0.1th and 99.9th percentiles of vertical velocity. The average cold point height is shown in the solid grey line while the 5th–95th (25th–75th) percentiles are shaded in light (dark) grey. All percentiles are taken over the 10°×10° TWP region and days 3–40 of the model run.

Appendix B

CONVECTIVE TIME SERIES FOR NICAM, ICON, AND SAM

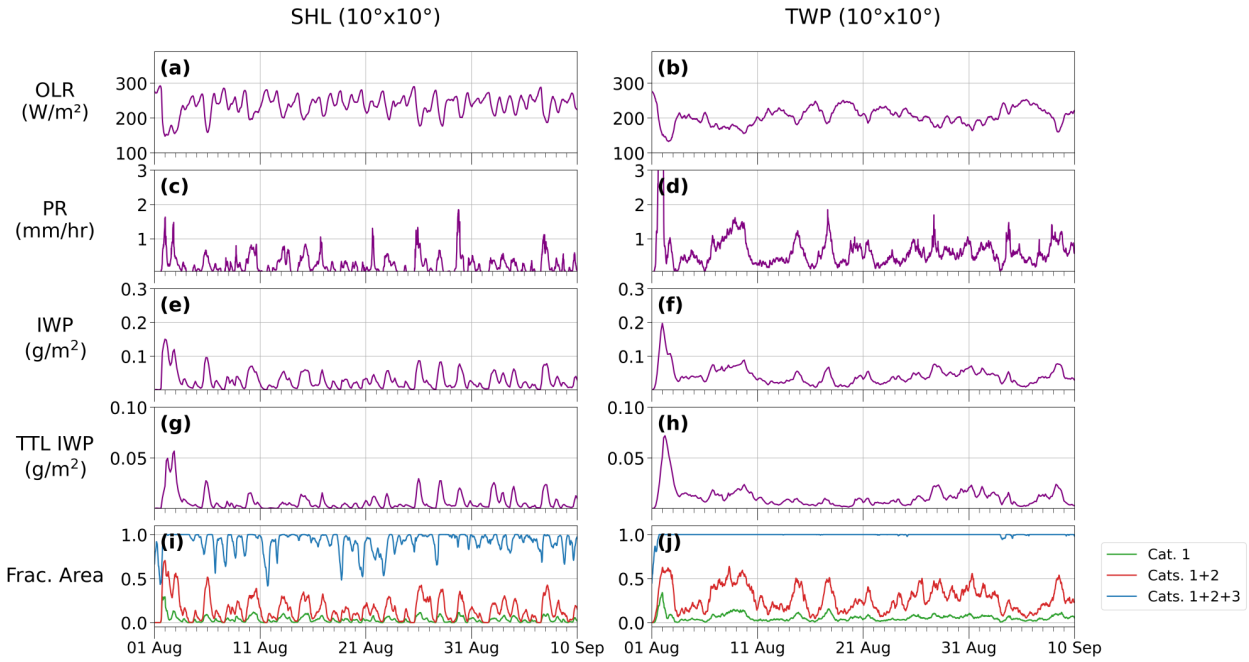

Figure B.1: Equivalent to Figure 5.1, but for NICAM. Time series for NICAM over days 1–40 of the model run: (a–b) area-mean outgoing longwave radiation (OLR); (c–d) area-mean precipitation rate (PR); (e–f) area-mean total column ice water path (IWP); (g–h) area-mean TTL IWP; and (i–j) fractional area of Category 1, Categories 1–2, and Categories 1–3 columns for FV3 over days 1–40 of the model run. Area-means and fractional areas are computed over the 10°×10° (left) Sahel and (right) TWP regions. For the TTL IWP, ice water content is integrated between the model levels closest to 14 and 18 km, which sometimes lie slightly outside of this range.

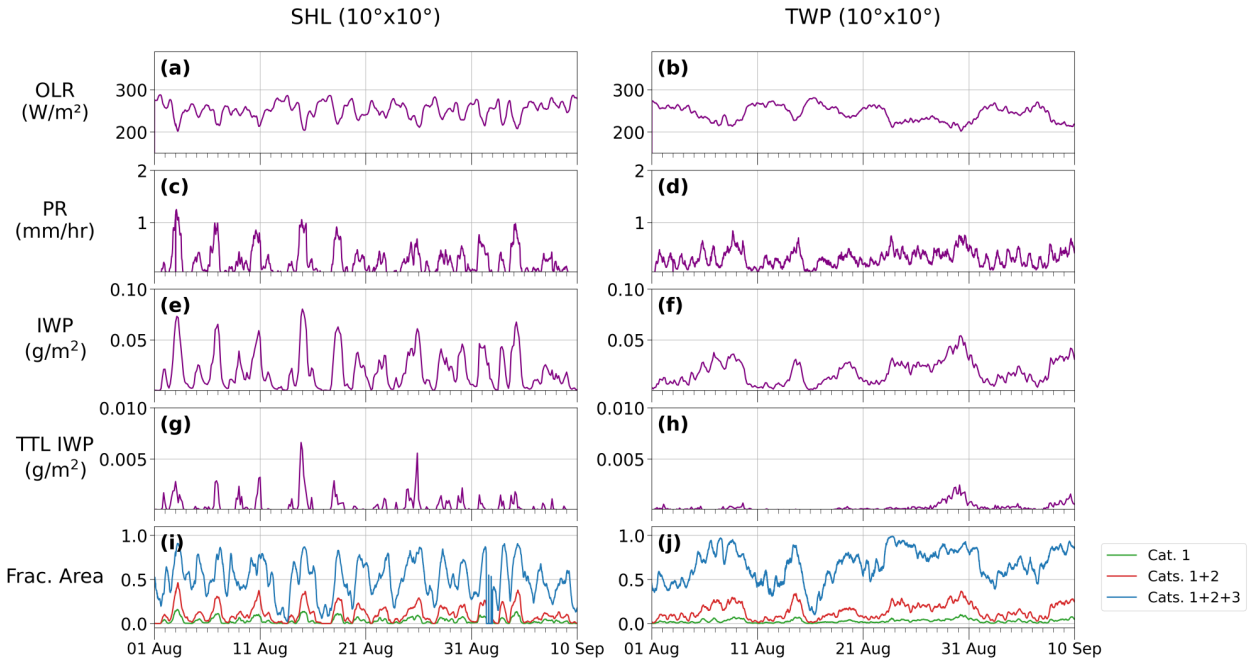

Figure B.2: As in Figure B.1, but for ICON.

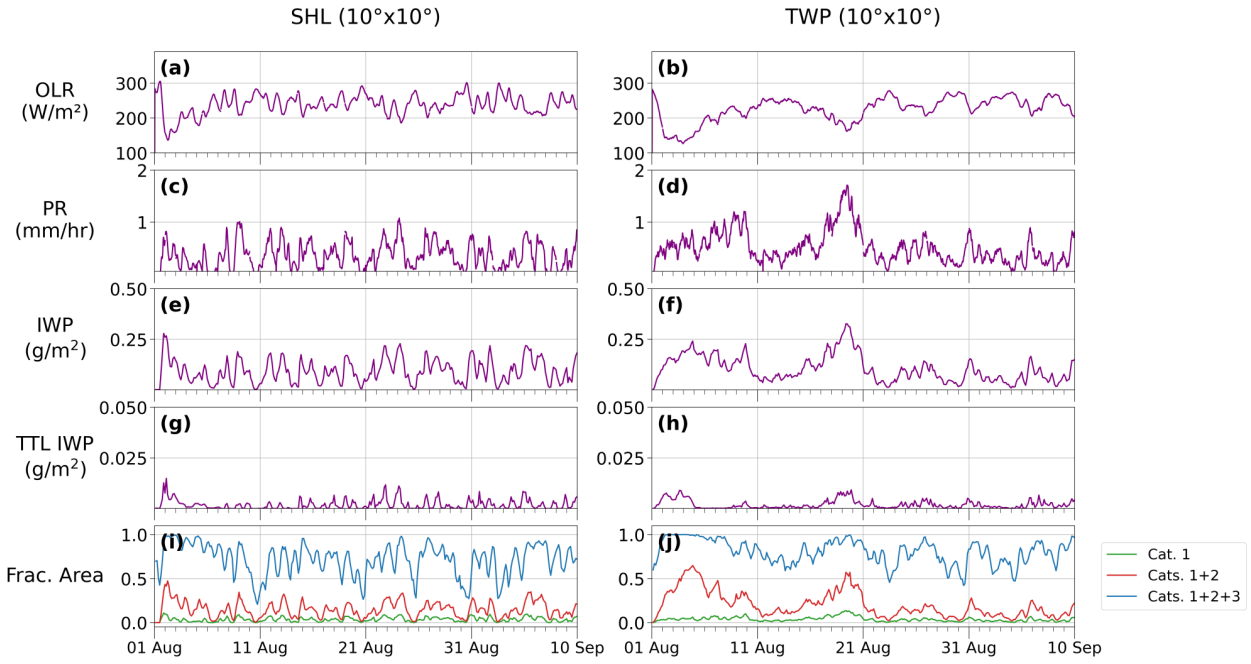

Figure B.3: As in Figure B.1, but for SAM.